Exploration of Planetary Hyperspectral Images with Unsupervised Spectral Unmixing: A Case Study of Planet Mars

Jun Liu, Bin Luo, Sylvain Douté, Jocelyn Chanussot

remote sensing

MDPI

Article

Exploration of Planetary Hyperspectral Images with Unsupervised Spectral Unmixing: A Case Study of Planet Mars

Jun Liu [1], Bin Luo [1,*], Sylvain Douté [2] and Jocelyn Chanussot [3,4]

[1] State Key Laboratory for Information Engineering in Surveying, Mapping and Remote Sensing, Wuhan University, 129 Luoyu Road, Wuhan 430079, China; liujunand@whu.edu.cn
[2] Institut de planétologie et d'astrophysique de Grenoble, CNRS, 38000 Grenoble, France; sylvain.doute@univ-grenoble-alpes.fr
[3] Université Grenoble Alpes, CNRS, Grenoble INP, GIPSA-lab, 38000 Grenoble, France; jocelyn.chanussot@gipsa-lab.grenoble-inp.fr
[4] Faculty of Electrical and Computer Engineering, University of Iceland, 101 Reykjavik, Iceland
* Correspondence: luob@whu.edu.cn

Received: 8 March 2018; Accepted: 7 May 2018; Published: 10 May 2018

Abstract: We propose to replace traditional spectral index methods by unsupervised spectral unmixing methods for the exploration of large datasets of planetary hyperspectral images. The main goal of this article is to test the ability of these analysis techniques to automatically extract the spectral signatures of the species present on the surface and to map their abundances accurately and with an acceptable processing time. We consider observations of the surface of Mars acquired by the imaging spectrometer OMEGA aboard MEX as a case study. The moderate spatial resolution (≈300 m/pixel at best) of this instrument implies the systematic existence of geographical mixtures possibly conjugated with non-linear (e.g., intimate) mixtures. We examine the sensitivity of a series of state-of-the-art methods of unmixing to the intrinsic spectral variability of the species in the image and to intimate assemblages of compounds. This study is made possible thanks to the use of well-controlled synthetic data and a real OMEGA image, for which the present icy species (water and carbon dioxide ices) and their characteristic spectra are widely known by the planetary community. Furthermore, reference maps of component abundances are built by the inversion of a more realistic physical model (simulating the propagation of solar light through the atmosphere and reflected back to the sensor) in order to validate the methods with the real image by comparison with the maps extracted by unmixing. The results produced by the processing pipeline of the eigenvalue likelihood maximization (ELM), vertex component analysis (VCA) and non-negativity condition least squares error estimators (NNLS) are the most robust to non-linear effects, highly-mixed pixels and different types of mixtures. Despite this fact, the produced results are not always the best because the VCA method assumes the existence of pure pixels in the image, that is pixels completely occupied by a single species. However, this pipeline is very fast and provides endmember spectra that are always interpretable. Finally, it produces more accurate distribution maps than the spectral index methods. More generally, the potential benefits of unsupervised spectral unmixing methods in planetary exploration is emphasized.

Keywords: hyperspectral image; spectral unmixing; Mars

1. Introduction

In the last two decades, visible and near-infrared imaging spectroscopy has proven to be crucial to study the Earth and other planets from orbit. Since its first appearance aboard a spacecraft in 1989,

this remote sensing technique has been used to study the surface and the atmosphere of Mars, Venus, Jupiter, Saturn, the Moon, etc. [1–8]. The main advantage of imaging spectroscopy is its ability to map the chemical composition and the physical state of planetary materials, thus providing clues about the geological and environmental evolution.

The OMEGA instrument (Observatoire pour la Minéralogie, l'Eau, les Glaces et l'Activité [9]) is an imaging spectrometer on board the Mars Express orbiter (European Space Agency). Since 2004, it has been mapping Mars with channels in the near-infrared spectral range (0.92–5.2 μm) and 96 channels in the visible and near-infrared range (0.36–1.0 μm). The OMEGA instrument provides a global coverage at a medium resolution (1–4 km) of the entire surface of Mars, as well as snapshots of selected areas with a resolution of a few hundreds of meters. OMEGA has provided a wealth of information concerning the composition and distribution of minerals and volatile species at the surface and in the atmosphere of Mars through the spectral analysis of the re-diffused solar light [10–13].

In the literature, the datasets collected by OMEGA have been exploited to map specific minerals or ices at the surface, even though such mapping is often performed in a relative sense. In particular, classical analyses by spectral index methods have been carried out for determining the spatio-temporal distribution of H_2O and CO_2 ices at the high latitudes of the red planet [12,14,15]. More generally, these rather simple methods require prior knowledge of the compounds expected on the scene and on their characteristic spectral signatures, such as the position and shape of the distinctive absorption bands. Nonetheless, it is often difficult to predict the existence of certain minerals or ices in the field of planetary exploration. Although many authors have proposed the use of laboratory measurements as reference signatures, planetary surface materials especially rocks and ices present reflectance spectra with a higher diversity than those observed in the laboratory [16]. Finally, spectral index methods discard most of the information enclosed in a hyperspectral image by reducing an entire spectrum to only a few channels, which can be subject to noise and other instrumental artifacts. In this context, although these techniques are simple to implement and numerically very efficient for exploring whole datasets, we propose to replace spectral index methods advantageously by unsupervised unmixing methods. The latter are widely used in terrestrial remote sensing [17]. The main contribution of this article is to test the ability of these analysis techniques in the planetary domain to automatically extract the characteristic spectral signatures of the present species at the ground level and to accurately map their abundances while preserving an acceptable processing time. Special attention is paid to the ices since the latter usually present distinct and strong absorption features that are especially suitable for unmixing. On the other hand, in most realistic situations, such species are highly mixed and present high intrinsic spectral variabilities (e.g., due to grain size effects).

Due to the wide application of spectral unmixing, many unmixing algorithms have been proposed according to the expected type of mixing [18,19]. Spectral mixing models can be characterized as either linear or nonlinear [20,21]. Current unsupervised unmixing methods mathematically model the spectral signal acquired by sensors based on a linear mixture model [22–25]. This widely-adopted assumption supposes that the spectrum of each pixel of a hyperspectral image is a linear mixture of some elementary chemical species (hereafter called endmembers). Based on the linear mixture assumption, it is indeed possible to extract the spectra of existent endmembers in a hyperspectral image and to process the spectrum of each pixel to obtain the corresponding abundance of each endmember. Both operations can be completed in an unsupervised way. Non-linear effects due to more complex mixtures may exist in a hyperspectral image because of intimate assemblages of compounds at the surface and multiple scattering between reflecting topographical facets, or between the latter and the atmosphere [26,27]. Three hyperspectral mixture models jointly with Bayesian algorithms for supervised hyperspectral unmixing have been introduced in [28]. Based on the residual component analysis model [29], the proposed general formulation assumes the linear model to be corrupted by an additive term whose expression can be adapted to account for nonlinearities (NL), endmember variability (EV) or mismodeling effects (ME). In [30], a proposed nonlinearity model generalizes RCA-nonlinearities model [28] by accounting for multiple scattering effects. Nevertheless, a linear

mixture model is considered to be adequate to realize a first exploration of the image, i.e., to identify and qualitatively map the existent materials [31,32].

The majority of linear spectral unmixing is based on dividing the whole process of linearly unmixing a given hyperspectral image into three sequential steps [33]: (i) the estimation of the number of endmembers; (ii) the extraction of the spectral signatures of the endmembers; and (iii) the computation of the abundances of the endmembers.

The first step consists of estimating the number of endmembers that exist in the image. This is one of the most essential parameters for the endmember extraction methods performed in the second step of spectral unmixing. For this purpose, thresholding techniques based on a principal component analysis are often used [31]. However, this rather simple strategy is limited as the cut-off threshold is not easy to determine because the eigenvalues related to the signal and the noise are often similar. More sophisticated approaches have been proposed in the literature and belong to two families. The first family is based on the eigenvalues of the covariance or correlation matrices of the data, such as the techniques referred to as Harsanyi–Farrand–Chan (HFC) [34] and eigenvalue likelihood maximization (ELM) [35]; the other is based on the minimization of the error when data are projected onto a given sub-space, such as the method referred to as hyperspectral signal identification by minimum error (HySime) [36].

The second step consists of extracting the representative spectra of the endmembers from a hyperspectral image. For this purpose, one can find three types of approaches (see Table 1): (i) statistical methods, (ii) non-negative matrix factorization (NMF) methods and (iii) geometrical methods. The statistical method referred to as principal component analysis (PCA) is classically used along with a linear mixture model to access the relevant information from planetary scenes [37]. Even though PCA permits pixel classification into distinct spectral types, it generally fails to provide automatically-interpretable spectral components (i.e., endmembers). On the other hand, independent component analysis (ICA) [38] has been proposed to extract the endmembers in a hyperspectral image by assuming that physical sources are non-Gaussian and mutually independent. Application of ICA on images acquired by the OMEGA hyperspectral imager allowed the retrieval of meaningful endmembers in [39]. Nonetheless, the role of ICA in carrying out spectral unmixing is questioned in [38], since the independence of the abundance distributions is not satisfied. Another important limitation of ICA is the potential unphysical results in the form of negative values affecting the extracted spectra or abundances. The unmixing problem has also been solved in a Bayesian framework through Bayesian positive source separation (BPSS) [40], ensuring a unique, robust solution. In [31], a combination of spatial ICA and BPSS applied on OMEGA data led to endmembers whose associated spectra and abundance maps correlated satisfactorily with reference signatures and the outcomes of physical models, respectively. However BPSS, based on Monte Carlo simulations, is quite computationally demanding. NMF [41] constitutes the basis of the second family of techniques by simultaneously finding the endmembers and abundance matrices whose product is the closer to the observed data, according to a given metric. Such a technique requires regularization to reduce the number of solutions. Several NMF-associated methods have been developed for spectral unmixing based on different practical constraints [42], such as the minimum volume [43], the sparse abundances [44], the low-rank property [45], the hypergraph structure [46], etc. As explained below, minimum-volume constrained non-negative matrix factorization (MVC-NMF), for example, considers the minimum-volume enclosing simplex as a constraint. The MiniDisCo-NMF algorithm [23] makes the assumption of minimum spectral dispersion for the regularization. The NMF approach has been used in planetary exploration to estimate the surface composition of Mars, using data acquired by the Martian rovers [47]. Geometrical approaches are contrarily based on the geometrical properties of the linear mixture model of hyperspectral data. Methods belonging to the third family are more adapted to the data and are generally more efficient. They can be divided into two sub-families: direct methods, including pixel purity index (PPI), N-Findr [48], vertex component analysis (VCA) [49] and sequential maximum angle convex cone (SMACC) [50]; and advanced methods, including MVC-NMF [44], minimum-volume

simplex analysis [51], minimum-volume enclosing simplex (MVES) [52] and simplex identification via split augmented Lagrangian (SISAL) [53]. Direct methods are very efficient as they extract the extremal points of the simplex formed by the data as endmembers. However, they assume that there is at least one pure pixel for each endmember in the image (the so-called pure pixel assumption). If this assumption is not satisfied, the extracted endmembers correspond to mixed spectra. On the other hand, advanced methods aim at either: (i) finding the simplex with the minimum volume that contains all the data points to extract the extremal points of the simplex as endmembers (e.g., MVSA, MVES and SISAL); or (ii) minimizing the projection error of the data to a subset and using the simplex volume as the regularization term (e.g., MVC-NMF). In the latter case, methods are considered to be hybrid as they are based on both geometric and NMF concepts. Advanced geometrical methods do not require the pure pixel assumption and may provide endmembers for which a pure sample does not exist in the image. Although these endmembers may be optimal from a mathematical point of view, their interpretation may become difficult as they may be unphysical [32]. In this article, two geometrical methods and one hybrid method are selected for the spectral unmixing of hyperspectral data because of their high efficiency. The following three representative methods are evaluated: VCA, representing the direct geometrical methods; SISAL, representing the advanced simplex volume optimization methods; and MVC-NMF, representing the factorization methods with the simplex volume condition.

Table 1. Categories of endmember extraction and unmixing methods. The methods marked with blue can be applied to endmember extraction, and methods marked with purple are suited for both endmember extraction and unmixing. PPI, pixel purity index.

Geometrical-Based Approaches		NMF Methods	Statistical Methods
pure pixel based	PPI [54] N-FINDR [48] SMACC [50] VCA [49]	MVC-NMF [44] $L_{1/2}$ sparsity-constrained NMF ($L_{1/2}$-NMF [55]) graph-regularized $L_{1/2}$-NMF (GLNMF [43]) MiniDisCo-NMF [23]	ICA [38] Bayesian approached [40]
minimum volume based	MVSA [51] MVES [52] MVC-NMF [44] SISAL [53]	subspace vertex pursuit-NMF (SVP-MNF [45]) hypergraph-regularized $L_{1/2}$-NMF (HG$L_{1/2}$-NMF [46])	

The last step aims at computing the abundances of the endmembers based on the extracted spectra by least squares estimators, subject to different conditions. In this article, two approaches have been considered: NNLS (non-negativity condition least squares error estimators) and FCLS (full condition least squares error estimators). The former estimates the abundances of the endmembers by assuming that the abundance values should be positive, while the latter assumes not only positivity, but also the unity of the sum of abundances on each pixel.

Since the main goal of this article is to evaluate the validity of the linear mixture model for unsupervised identification and mapping of ices and, to a lesser extent, the minerals that are found on the planet Mars, based on images acquired by the instrument OMEGA, we focus on a polar case study implying compounds such as CO_2, H_2O and mineral dust. The reason for this choice is the availability of large time series of OMEGA observations acquired above the Martian poles and the numerous, distinctive and often overlapping absorption bands that characterize the icy materials on Mars. In addition, a full analysis of their spectra by the inversion of reflectance radiative transfer models is sometimes feasible [56–58], even though such a type of analysis requires substantially more numerical effort. In this article, the physical approach provides reference maps in order to validate the considered methods for dataset exploration.

The plan of this article is as follows. In Section 2, we briefly present the concept of unsupervised linear unmixing, including the linear mixture model, the methods for estimating the number of endmembers, the methods for extracting the endmembers, as well as the approaches for decomposing the spectra of the pixels in a hyperspectral image. In Section 3, we present the experiments and the results obtained with synthetic data that validate the unsupervised scheme of linear unmixing.

In Section 4, the experiments and results obtained on real OMEGA data are detailed. We draw our conclusions in the final section.

2. The Methodology of Linear Unmixing

In this section, we introduce the methodology of unsupervised linear unmixing for hyperspectral images. The unmixing of a hyperspectral image is based on the linear mixture model, which is introduced in Section 2.1. For the first step, which is the estimation of the number of endmembers, we evaluate the HFC, ELM and HySime methods. They are briefly introduced in Section 2.2. For the second step, which is the extraction of endmembers, we evaluate the VCA, SISAL and MVC-NMF methods, for which brief introductions are presented in Section 2.3. For the final step (computing the abundances of the endmembers), we evaluate NNLS and FCLS, which are introduced in Section 2.4.

2.1. The Linear Mixture Model

We note that $\mathbf{X}$ is the matrix representing the hyperspectral image cube, where $\mathbf{X} = \{\mathbf{x}_1, \mathbf{x}_2, \ldots, \mathbf{x}_{N_a}\}$ and $\mathbf{x}_k = \{x_{1,k}, x_{2,k}, \ldots, x_{N_s,k}\}^T$, $x_{l,k}$ is the value of the k-th pixel at the l-th band, N_s is the number of spectral bands and N_a is the number of pixels. We assume that the spectrum of each pixel is a linear mixture of the spectra of N_c endmembers, leading to the following model:

$$\mathbf{X} = \mathbf{MS} + \mathbf{n} \tag{1}$$

where $\mathbf{M} = \{\mathbf{m}_1, \mathbf{m}_2, \ldots, \mathbf{m}_{N_c}\}$ is the mixing matrix, where $\mathbf{m}_n$ denotes the spectral signature of the n-th endmember. $\mathbf{S} = \{\mathbf{s}_1, \mathbf{s}_2, \ldots, \mathbf{s}_{N_c}\}^T$ is the abundance matrix, where $\mathbf{s}_n = \{s_{n,1}, s_{n,2}, \ldots, s_{n,N_a}\}$ ($s_{n,k} \in [0,1]$ is the abundance of the n-th endmember at the k-th pixel). $\mathbf{n}$ stands for the additive noise of the image. For separating $\mathbf{M}$ and $\mathbf{S}$ from $\mathbf{X}$ without any a priori information, we first have to estimate the number N_c of endmembers. In the second step, we can perform a linear unmixing of $\mathbf{X}$ in order to obtain $\mathbf{M}$ and $\mathbf{S}$.

2.2. Estimation of the Number of Endmembers

In this section, we briefly present the two families of methods for estimating the number of endmembers: the methods based on the eigenvalues of the covariance and correlation matrices (including HFC and ELM) and the methods based on the minimization of the linear projection errors (the HySime methods).

Harsanyi–Farrand–Chan

According to the linear mixture model of Equation (1), we note that K is the sample covariance matrix of $\mathbf{X}$ and R is its correlation matrix. Suppose that λ_i and $\hat{\lambda}_i$ are the i-th eigenvalues of K and R, respectively, with $i \geq 0$, $\lambda_i > \lambda_{i+1}$ and $\hat{\lambda}_i > \hat{\lambda}_{i+1}$. Theoretically, if there are N_c endmembers present in $\mathbf{X}$, the eigenvalues $\hat{\lambda}_i, (i > N_c)$ and $\lambda_i, (i > N_c)$ correspond to the noise variance. We therefore have:

$$\begin{cases} \hat{\lambda}_i - \lambda_i > 0, & i \leq N_c \\ \hat{\lambda}_i - \lambda_i = 0, & i > N_c \end{cases} \tag{2}$$

Noting $z_i = \hat{\lambda}_i - \lambda_i$, the HFC method presented in [34] uses a Neyman–Pearson test [59] to threshold the z_i value in order to estimate the number of endmembers.

Eigenvalue Likelihood Maximization

The HFC method needs to fix the false alarm value α in order to determine the threshold for z_i, which can affect the estimated number of endmembers.

In [35], it was proposed to use the distribution of the z_i values for estimating the number of endmembers without any parameter, which can give a precise number of endmembers, even if the SNR is very low. According to [60], the distribution of z_i can be modeled by:

$$\begin{array}{ll} z_i \sim \aleph(\mu_i, \sigma_i^2), & i \leq N_c \\ z_i \sim \aleph(0, \sigma_i^2), & i > N_c \end{array} \tag{3}$$

where $\aleph$ is the symbol for a Gaussian probability distribution function, μ_i is unknown and σ_i can be given by $\sigma_i^2 \approx \frac{2}{N}(\hat{\lambda}_i^2 + \lambda_i^2)$, if the number of samples is sufficiently large (which is usually the case for hyperspectral images) [60].

According to Equation (3), we can define a likelihood function:

$$H(i) = \Pi_{l=i}^{N_s} \frac{1}{\sigma_l} \exp(-\frac{z_l^2}{2\sigma_l^2})$$

and we take its logarithmic value:

$$\tilde{H}(i) = \log H(i) = -\sum_{l=i}^{N_s} \frac{z_l^2}{2\sigma_l^2} - \sum_{l=i}^{N_s} \log \sigma_l. \tag{4}$$

According to [35], the number of endmembers is given by:

$$\hat{N}_c = \arg\max_i \{\tilde{H}(i)\} - 1 \tag{5}$$

Hyperspectral Signal Identification by Minimum Error

HySime, as proposed in [36], consists of two steps: the estimation of the noise **n** and the estimation of N_c by projecting the data into a sub-space. For estimating the noise, the authors consider that one given spectral band of a hyperspectral image can be obtained by a linear regression of the adjacent bands. The difference between the reconstructed band and the original band is the estimated noise.

According to [36], the number of endmembers corresponds to the dimension of the sub-space, which minimizes the mean square errors between the denoised original data and the projected one.

2.3. Endmember Extraction

According to the linear mixture model presented in Section 2.1, if the data are noise free, all the hyperspectral data are contained inside a simplex, of which the extrema are the endmembers. The geometrical methods for endmember extraction use this property and extract the extremes of the simplex as endmembers. As mentioned in the Introduction, the direct methods, such as VCA, N-Findr and SMACC, require the pure pixel assumption. Since pure pixels do not always exist in a hyperspectral image, advanced methods, such as SISAL, MVES, MVSA, MVC-NMF, etc., are proposed in order to find the real endmembers in case they are not present in the image. However, it should then be noted that they could be more difficult to physically interpret than the endmembers extracted by direct methods, which always exist in the image.

In this article, we select VCA to represent the direct methods. Simplex identification via split augmented Lagrangian (SISAL) and minimum-volume constrained non-negative matrix factorization (MVC-NMF) are selected to represent the advanced methods SISAL, being based on simplex optimization, while MVC-NMF is based on non-negative matrix factorization with an optimal simplex as the regularization term.

Vertex Component Analysis

VCA, as proposed in [49], is a very efficient method for extracting endmembers that are linearly mixed. VCA iteratively projects the data onto the direction orthogonal to the sub-space spanned by

the endmembers already determined. The extreme of this projection is the new endmember signature. The algorithm stops the iteration when all the N_c endmembers are extracted, where N_c is the number of endmembers, which has to be fixed before performing VCA.

Simplex Identification via Split Augmented Lagrangian

SISAL has recently been proposed to solve the linear unmixing of the minimum-volume simplex [53]. Being a non-convex optimization problem with convex constraints, the positivity constraints are replaced by soft constraints, forcing the spectral vectors to belong to the convex hull of the endmember signatures. The resulting problem is solved by a sequence of augmented Lagrangian optimizations. SISAL is fast, and its effectiveness has been tested on simulated data. Unlike VCA, the extrema of the simplex obtained by SISAL may not be present in the hyperspectral image; thus, SISAL does not assume the presence of pure pixels.

Minimum-Volume Constrained Non-Negative Matrix Factorization (MVC-NMF)

MVC-NMF is proposed for endmember extraction of highly-mixed hyperspectral data, without the pure pixel assumption [44]. This method decomposes mixed pixels by analyzing the connection between the spectral unmixing analysis and the non-negative matrix factorization. Injecting the constraint of the minimum volume of the simplex as a regularization term of the non-negative matrix factorization, MVC-NMF is less dependent on the initializations, robust to different levels of noise, less sensitive to the estimated number of endmembers and applicable to images with or without pure pixel representations.

Because the advanced statistical method BPSS applied to images of Mars [31,32] has already led to very satisfactory results, we use the latter as a reference to which we compare the outcomes of the previous methods in Section 4.

Bayesian Positive Source Separation

BPSS proposes to estimate the matrices M and S in a Bayesian framework under a linear model with inherent positivity and additivity constraints and no pure pixel assumption [40]. In BPSS, the noise, S and M are assumed to follow Gaussian, Dirichlet and Gamma probability density functions, respectively. The method of BPSS is based on hierarchical Bayesian models to encode prior information regarding the parameters of interest. The complexity of the estimation from the resulting posterior distribution is overcome using Markov chain Monte Carlo methods. In BPSS, the degree of uncertainty affecting the extracted endmember spectra can be estimated as the results are computed as probability distribution functions.

2.4. Linear Unmixing of Hyperspectral Images

Based on the spectra of the extracted endmembers, the abundances of each can be estimated by unmixing the image based on least squares error estimators, with the following conditions:

- unconditioned (UCLS), which directly solves the following equation:

$$\hat{\mathbf{S}}_{Ucls} = \arg\min_{\mathbf{S}} ||\mathbf{X} - \mathbf{MS}||^2, \tag{6}$$

- subject to the non-negativity condition (NNLS), which solves the following equation:

$$\begin{aligned} \hat{\mathbf{S}}_{Nnls} &= \arg\min_{\mathbf{S}} ||\mathbf{X} - \mathbf{MS}||^2, \\ s.t. \quad \mathbf{S} &\geq 0 \end{aligned} \tag{7}$$

- subject to both the non-negativity condition and the sum-to-one condition (FCLS) [61], which solves the following equation:

$$\begin{aligned} \hat{\mathbf{S}}_{Fcls} &= \arg\min_{\mathbf{S}} ||\mathbf{X} - \mathbf{MS}||^2, \\ s.t. \quad \mathbf{S} &\geq 0 \quad and \quad \sum_{n=1}^{N_c} s(n,k) = 1 \end{aligned} \tag{8}$$

We mainly focus on linear unmixing models in this article. Nevertheless, we also consider the recent multilinear mixing model [62,63] in the comparative experiment (Section 4). In the following, we abandon examining the UCLS condition since it can lead to unphysical negative values for the abundances.

2.5. Performance Metrics

To assess the performance of spectral unmixing models, four quantitative criteria, spectral angle mapper (SAM), reconstruction error (RE), correlation coefficients and mean square error (MSE), will be applied. SAM is used to measure the spectral distortion between the actual and estimated endmembers and is defined as the following equation:

$$SAM(e_n, \hat{e}_n) = arcos(\frac{(e_n, \hat{e}_n)}{\|e_n\|_2 \|\hat{e}_n\|_2}) \tag{9}$$

where e_n is the reference spectral signature and $\hat{e}_n$ is the estimated endmember. To evaluate how well different spectral unmixing models fit the observed data, the reconstruction error (RE) is computed as Equation (10):

$$RE = \|\hat{X} - X\|_F \tag{10}$$

where $\hat{X}$ is the reconstructed data from spectral unmixing model. The smaller RE, the better the model fits the data. We choose correlation coefficients between the reference abundances and the abundances of the identified endmembers as the third quantitative criterion, which is computed according to Equation (11):

$$\rho(A_i, \hat{A}_i) = \frac{Cov(A_i, \hat{A}_i)}{\delta_{A_i} \delta_{\hat{A}_i}} \tag{11}$$

where A_i is the reference abundance and $\hat{A}_i$ is the estimated abundance. The larger the correlation coefficients, the higher the accuracy of the estimated abundance. Moreover, the correlation coefficients also can be used to evaluate the performance of the endmember extraction. The last performance metric we consider is the MSE:

$$MSE(A_i, \hat{A}_i) = \frac{1}{N_p} \|A_i - \hat{A}_i\|_F \tag{12}$$

where N_p is the number of pixels. The smaller the MSE, the better the quality of the estimation.

3. Sensitivity Study

In this section, we evaluate the sensitivity of the unmixing approaches with regard to several aspects by using well-controlled synthetic datasets (see Table 2). In Section 3.1, the sensitivity to the degree of mixing of the endmembers is evaluated. In Section 3.2, the sensitivity to the variations in the spectra of the endmembers caused by non-linear effects is studied.

3.1. Sensitivity with Regard to the Degree of Mixing: Experiments and Results with Synthetic Data

This experiment is carried out based on synthetic data simulated according to the linear mixture model presented in Section 2.1. Since the spatial resolution of the images acquired by the OMEGA instrument is relatively moderate (typically one kilometer), we cannot be assured that there are pure pixels for each endmember. The purpose of this experiment is to evaluate the efficiency of the endmember extraction methods when the pixels are highly mixed. We use the synthetic spectra of three typical materials present on the south pole of Mars (H_2O, CO_2 and dust [10]) for generating the synthetic data. The main chemical composition of dust is fine-grain iron(III) oxide [64,65].

The reference spectra of the three endmembers are simulated by a surface reflectance model [13] and are shown in Figure 1 . Note that the spectrum of the dust endmember is affected by atmospheric absorption. The noise is additive Gaussian, and the SNRis set to 20 dB, which is in the lower half of the typical range of SNR variations in the images acquired by the OMEGA instrument. The abundances of these endmembers are simulated following a Dirichlet distribution, which allows us to set the maximal abundance of each endmember. In this experiment, our aim is to evaluate the performances of the three endmember extraction methods when the endmembers are highly mixed. The maximal abundance of each endmember varies from 0.6–1, with an increment of 0.2.

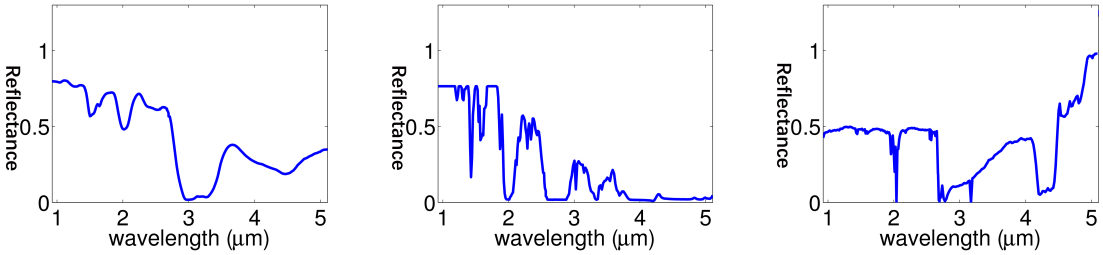

(**a**) Water ice (**b**) CO_2 ice (**c**) Dust

Figure 1. Reference spectra of three typical Mars components calculated by numerical modeling.

We then compute the correlation coefficient and the spectral angle between the spectra of the extracted endmembers and the reference spectra simulated in the laboratory. Ideally, for a given compound, the extracted endmember that has the maximal correlation coefficients and the minimal spectral angle can be associated with this compound. We must note that, if the sources are correctly extracted for the current experiment, the abundance retrieval is necessarily satisfactory because we exactly use the linear model to generate and unmix the data.

The correlation coefficients between the reference spectra of the compounds and the identified extracted endmembers are shown in Table 3. When the endmembers are moderately to not highly mixed, i.e., the maximal abundance of each endmember is between 0.7 and one, the extracted endmembers by the three methods can be easily identified. It can be seen that the SISAL method always gives the best results, while the results of the VCA and MVC-NMF methods are degraded to approximately the same level. When the endmembers are highly mixed (i.e., maximal abundances equal to 0.6), the performance of SISAL declines dramatically. Meanwhile, the results of VCA are quite stable, and the results of MVC-NMF are similar to the former. Thus, in the highly-mixed case, the SISAL method, which does not require the pure pixel assumption, can extract distorted endmembers that are unphysical. In all likelihood, SISAL will then not be robust against the presence of outlier spectra and of significant levels of noise for some channels. In contrast, the MVC-NMF method based on the same principles is more robust. On the other hand, because the VCA method is based on the pure pixel assumption, it always extracts endmembers that exist in the image; they are then more likely to be approximately relevant, even though they are actually mixed spectra.

From this experiment, we can conclude that the performance of VCA is not always the best one, due to its requirement for the pure pixel assumption. However, it is the most robust method with

regard to a high degree of mixing. In contrast, the SISAL method provides the best results in general, except when the endmembers are highly mixed (i.e., the maximal abundance of each endmember is 0.6). The MVC-NMF method always gives intermediate results.

Table 2. Characteristics of the datasets.

Dataset	Synthetic Dataset I	Synthetic Dataset II	ORB0041 Image
spatial size	21 × 1500	21 × 1500	300 × 128
spectral size	256 bands	256 bands	183 bands (eliminated 72 absorption bands)

Table 3. Correlation coefficients (CC) and spectral angles (SA) between the reference spectra and the spectra of the endmembers extracted by VCA, SISAL and MVC-NMF when the maximal abundances of the endmembers range from 0.6–1.

Maximal Abundance	Method	H_2O	CO_2	Dust
1	VCA [49]	1.000	1.000	1.000
	SISAL [53]	1.000	1.000	1.000
	MVC-NMF [44]	1.000	1.000	1.000
0.8	VCA [49]	0.987	0.990	0.970
	SISAL [53]	0.998	0.999	0.997
	MVC-NMF [44]	0.995	0.994	0.986
0.6	VCA [49]	0.970	0.969	0.820
	SISAL [53]	0.574	0.939	0.865
	MVC-NMF [44]	0.919	0.906	0.937

3.2. Sensitivity with Regard to Non-Linear Effects: Experiments and Results with Synthetic Data

In this section, we again simulate a linear mixture of spectra corresponding to three typical compounds present on the surface of the south pole of Mars , according to typical observation conditions and to the properties of the OMEGA instrument. However, this time, we apply spectral non-linear effects caused by the variations in the acquisition geometry and in the grain sizes of the materials. The incidence angle θ varies from 45 degrees–85 degrees, with an increment of two degrees. The grain sizes G of the three materials vary according to ranges typical of Martian conditions and are tabulated in Table 4. Similar parameter values were used for simulating the materials on the polar regions of Mars in [66]. The spatial distributions of these parameters (shown in Figure 2) reflect the fact that we consider all possible combinations of their values for simulating the synthetic data. The spectra of the three endmembers (when the incidence angles and the grain sizes form combinations of extremal values) are shown in Figure 3. For of clarity, we note these spectra by the notations shown in Table 5. As illustrated by Figure 2, different acquisition geometries and material granularities change the radiative transfer of solar light within the surface according to the wavelength, and this affects the calculated reflectance spectra. Some remarks can be drawn accordingly:

- For H_2O ice, the grain size causes the most variation. The most different spectra are $M^2_{H_2O}$ and $M^3_{H_2O}$. The correlation coefficient between these two spectra is only 0.830.
- For CO_2 ice, the spectral shapes under different conditions remain quite similar. Although the most different spectra are $M^2_{CO_2}$ and $M^3_{CO_2}$, the correlation coefficient between them is 0.987.
- For *dust*, the shapes of all the spectra are extremely similar. Even though the spectra M^2_{Dust} and M^3_{Dust} are the most different, their correlation coefficient is 0.994.

Additive noise has been simulated according to the SNR characteristic of the OMEGA instrument.

Table 4. Grain sizes of the three endmembers in the synthetic data.

Endmember	H_2O	CO_2	Dust
minimal grain size (μm)	100	45,000	25
maximal grain size (μm)	1000	60,000	30
increment (μm)	200	5000	2.5

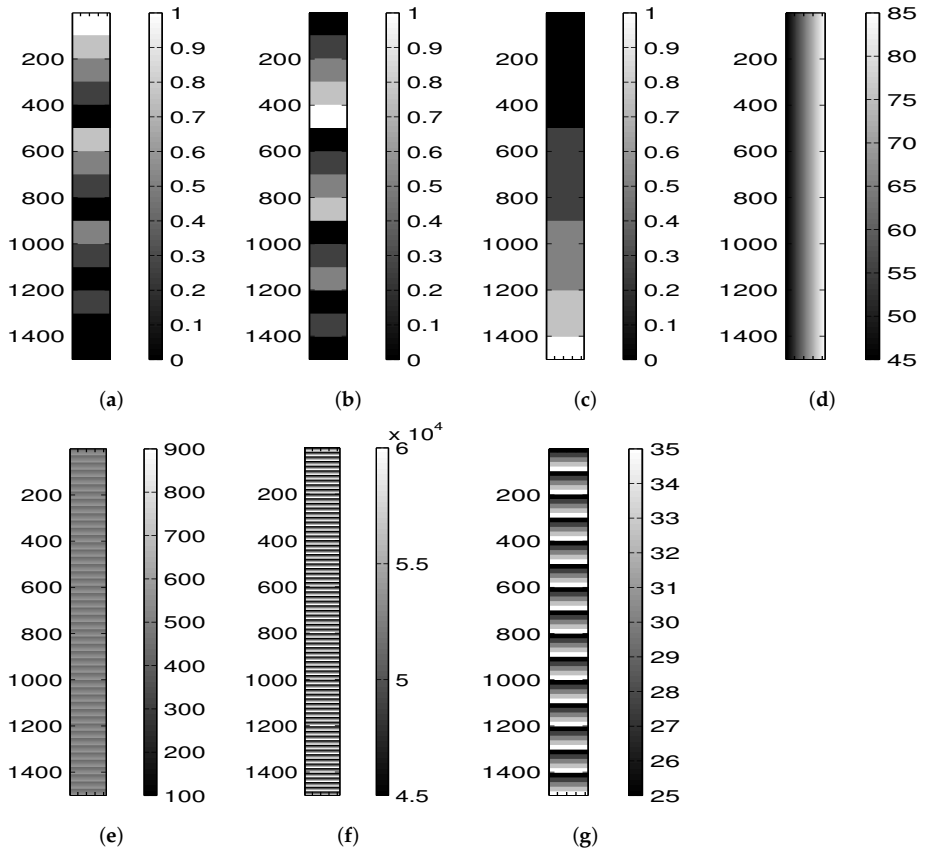

Figure 2. The spatial distribution of the parameters for simulating the synthetic data. The dimension of each image is 21 × 1500 pixels. For visualization, all the values of these parameters are normalized to [0, 255]. The scale of the parameters related to the gray values in the image are shown on the color bars to the right of each image. (**a**) Abundance of H_2O ice; (**b**) abundance of CO_2 ice; (**c**) abundance of dust; (**d**) solar angle θ (in degrees); (**e**) grain sizes G of H_2O ice; (**f**) grain sizes G of CO_2 ice; (**g**) grain sizes G of dust.

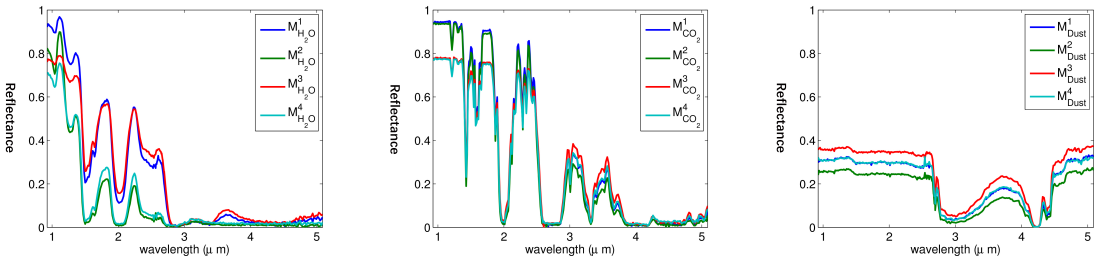

Figure 3. Spectral variations of the three endmembers (H_2, CO_2 and dust) caused by different solar angles (θ) and different grain sizes (G). The spectra are shown when the two parameters form a combination of extreme values.

Table 5. Notations of the spectra of the three endmembers with variations caused by different observation geometries and grain sizes.

Notation	Endmember	Grain Size G	Incidence Angle θ
$M^1_{H_2O}$	H_2O	45	100
$M^2_{H_2O}$	H_2O	45	900
$M^3_{H_2O}$	H_2O	85	100
$M^4_{H_2O}$	H_2O	85	900
$M^1_{CO_2}$	CO_2	45	45,000
$M^2_{CO_2}$	CO_2	45	60,000
$M^3_{CO_2}$	CO_2	85	45,000
$M^4_{CO_2}$	CO_2	85	60,000
M^1_{Dust}	Dust	45	25
M^2_{Dust}	Dust	45	35
M^3_{Dust}	Dust	85	25
M^4_{Dust}	Dust	85	35

3.2.1. Estimation of the Number of Endmembers

The methods ELM, HySime and HFC have been used for estimating the number of endmembers N_c of the synthetic data. The HFC method requires the false alarm parameter α. It has been set as 10^{-3}, 10^{-4} and 10^{-5} for our experiments. These values are suggested in [34]. Besides, our experiments show that when this value continues to decrease, it does not particularly affect the estimated number of endmembers. The results of the three methods are shown in Table 6.

Table 6. Number of endmembers estimated by the use of ELM, hyperspectral signal identification by minimum error (HySime) and HFC.

Method	ELM [35]	HySime [36]	HFC [34] $\alpha = 10^{-3}$	HFC [34] $\alpha = 10^{-4}$	HFC [34] $\alpha = 10^{-5}$
N_c	5	12	18	17	17

It can be seen that the numbers estimated by the HySime and HFC methods are much larger than the real number of physical sources (i.e., three). In such cases, the analysis of the extracted endmembers turns into a rather unfeasible task. The reason for this result may come from the higher sensitivity of HySime and HFC to subtle contributions in the image, such as the detection of residual artifacts, which could be valuable in other situations, but are out of the scope of this article. Therefore, these two methods are not further considered in this section. On the other hand, the ELM technique detects the presence of five endmembers. This result corresponds more satisfactorily to the chosen physical scenario, even though it is slightly biased. In accordance with what was observed in Figure 3, the H_2O grain size differences produce larger spectral differences than the CO_2 and *dust* grain sizes. The grain size differences are also more important than the acquisition geometry. Note that the correlation coefficient between the most different spectra of the water ice is only 0.803. Therefore, a pure component may lead to several endmembers, according to its intrinsic spectral variability, which is a non-linear function of its properties. This assumption will also be validated by the extraction of the endmembers.

3.2.2. Extraction of Endmembers

VCA, SISAL and MVC-NMF are then used for extracting the five endmembers from the synthetic image, for which the spectra are shown in Figure 4. The abundances of these endmembers are computed respectively by using NNLS and FCLS (see Equations (7) and (8)) , which are quite similar. The major difference is the contrast of the abundance maps. We then compare the extracted spectra

(Figure 4) with the reference spectra of the endmembers under different conditions (Figure 3) by computing the correlation coefficients between them. The coefficient values are shown in Table 7.

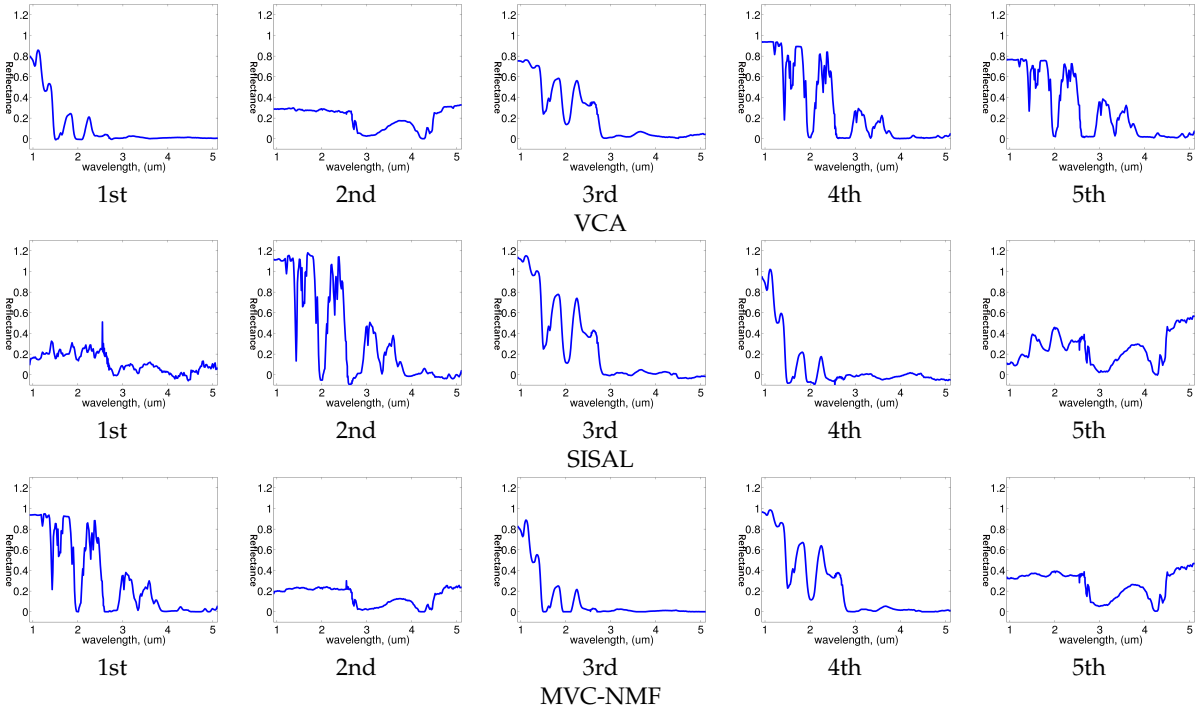

Figure 4. The spectra of the five endmembers extracted by VCA, SISAL and MVC-NMF with the synthetic data.

For the endmembers extracted by VCA, the first and the third endmembers correspond very well to $M^2_{H_2O}$ (water ice when the incidence angle $\theta = 45$ degrees and the grain size $G = 900$) and $M^3_{H_2O}$ (water ice when the incidence angle $\theta = 85$ degrees and the grain size $G = 100$). The fourth and the fifth endmembers perfectly (with correlation coefficients equal to one) correspond to $M^2_{CO_2}$ (CO_2 ice when $\theta = 45$ and $G = 60{,}000$) and $M^3_{CO_2}$ (CO_2 ice when $\theta = 85$ and $G = 45{,}000$). The second endmember corresponds very well to M^1_{Dust} (*dust* ice when $\theta = 45$ and $G = 25$). The extracted endmembers and the reference spectra are very well correlated (correlation coefficients are always higher than 0.995).

However, SISAL extracts endmembers that are not always interpretable. The 2nd, 3rd and the 4th endmembers can be identified respectively as $M^4_{CO_2}$ (CO_2 ice when $\theta = 85$ and $G = 60{,}000$), $M^1_{H_2O}$ (water ice when $\theta = 45$ and $G = 100$) and $M^2_{H_2O}$ (water ice when $\theta = 45$ and $G = 900$). However, we cannot make a physical interpretation for the first and the fifth endmembers, even considering their abundances. This may due to the fact that since the SISAL method does not require the pure pixel assumption, it may extract non-existing endmembers in the image, which cannot be physically interpreted.

Physical interpretations of the spectra extracted by MVC-NMF are more satisfactory than in the SISAL case. There are always two endmembers corresponding to H_2O ice of large and small grain size (respectively, $M^1_{H_2O}$ and $M^2_{H_2O}$). In contrast to the results of VCA, there is only one endmember that corresponds to CO_2 ice, and there are two endmembers corresponding to dust, differing only by their incidence angles (respectively, M^1_{Dust} and M^3_{Dust}).

Table 7. Correlation coefficients between the extracted endmembers by the use of VCA, SISAL and MVC-NMF and the reference spectra of the endmembers under different non-linear spectral effects. A bold face stresses, in each case, the best result.

Endmember	$M^1_{H_2O}$	$M^2_{H_2O}$	$M^3_{H_2O}$	$M^4_{H_2O}$	$M^1_{CO_2}$	$M^2_{CO_2}$	$M^3_{CO_2}$	$M^4_{CO_2}$	M^1_{Dust}	M^2_{Dust}	M^3_{Dust}	M^4_{Dust}
VCA [49]												
1st	0.907	**0.998**	0.835	0.996	0.718	0.733	0.677	0.692	0.397	0.411	0.384	0.399
2nd	0.552	0.372	0.596	0.406	0.460	0.465	0.439	0.449	**0.995**	0.992	0.994	0.993
3rd	0.987	0.822	**0.999**	0.870	0.861	0.866	0.840	0.849	0.648	0.664	0.640	0.656
4th	0.861	0.730	0.865	0.775	0.999	**1.000**	0.988	0.994	0.512	0.531	0.503	0.517
5th	0.823	0.670	0.836	0.719	0.993	0.986	**1.000**	0.998	0.484	0.501	0.474	0.489
SISAL [53]												
1st	0.626	0.308	0.710	0.376	0.613	0.594	0.653	0.636	0.703	0.710	0.694	**0.711**
2nd	0.800	0.664	0.808	0.710	0.995	0.992	0.994	**0.996**	0.449	0.467	0.439	0.453
3rd	**0.996**	0.868	0.995	0.910	0.856	0.864	0.830	0.841	0.589	0.606	0.580	0.596
4th	0.866	**0.994**	0.784	0.984	0.676	0.692	0.630	0.647	0.319	0.333	0.306	0.320
5th	−0.221	−0.354	−0.157	−0.343	−0.228	−0.228	−0.232	−0.229	0.637	0.620	**0.646**	0.630
MVC-NMF [44]												
1st	0.838	0.697	0.847	0.745	**0.999**	0.997	0.996	0.999	0.489	0.507	0.479	0.494
2nd	0.518	0.280	0.583	0.325	0.455	0.454	0.451	0.453	**0.984**	0.983	0.980	0.984
3rd	0.905	**0.998**	0.833	0.996	0.722	0.737	0.680	0.696	0.393	0.408	0.381	0.395
4th	**0.997**	0.866	0.996	0.908	0.857	0.864	0.831	0.842	0.608	0.624	0.599	0.615
5th	0.393	0.202	0.449	0.236	0.313	0.315	0.298	0.305	0.966	0.958	**0.970**	0.963

3.2.3. Extraction of the Abundances

The abundances of the endmembers extracted by VCA and MVC-NMF (the ones obtained by SISAL are not taken into consideration as the physical interpretations of their spectra cannot be completed) are then computed by using NNLS and FCLS. In order to confirm the identification of the endmembers, the estimated abundances are compared to the real abundances used for simulating the synthetic data. In any case, the spectral unmixing of the synthetic data is affected by source splitting effects linked to the non-linear spectral effects, thus making necessary the recombination of the five endmembers into three physical sources. After assigning each extracted endmember to one of the three physical sources, the abundance map of a given physical source is obtained by adding the individual abundances of the associated endmembers. The reconstructed maps are not displayed here to save space.

We note that $\mathbf{s}_n$ is the computed abundance of the n-th endmember. In addition, we recall that the first and third endmembers extracted by VCA are identified as H_2O ice, the fourth and fifth endmembers as CO_2 ice and the second endmember as dust. Therefore, the abundances of H_2O ice, CO_2 ice and dust are, respectively, $\mathbf{s}_1 + \mathbf{s}_3$, $\mathbf{s}_4 + \mathbf{s}_5$ and $\mathbf{s}_2$. For the endmembers extracted by MVC-NMF, the abundances of H_2O ice, CO_2 ice and dust are, respectively, $\mathbf{s}_3 + \mathbf{s}_4$, $\mathbf{s}_1$ and $\mathbf{s}_2 + \mathbf{s}_5$. In Table 8, we show the correlation coefficients and the mean square error between the real abundances of H_2O ice, CO_2 ice and dust (see Figure 2a–c) and the reconstituted abundances of the physical sources from the VCA and MVC-NMF results.

According to Table 8, it can be seen that the abundances of the physical sources reconstituted from the VCA results are always more closely correlated to the real abundances, no matter what estimator we use (NNLS or FCLS). The mean square errors obtained by VCA are also smaller. Within the abundances of the endmembers extracted by VCA, the results of the two estimators (NNLS and FCLS) are very close.

Table 8. Correlation coefficients and the mean square error between the real abundances of H_2O ice, CO_2 ice and dust, reconstruction error (RE) and the time cost of each method and the abundances of the endmembers extracted by VCA and MVC-NMF.

	Correlation Coefficients			**Mean Square Error**			**RE**	**Time (s)**
	H_2O Ice	**CO_2 Ice**	**Dust**	**H_2O Ice**	**CO_2 Ice**	**Dust**		
VCA [49] + NNLS	0.9924	0.9988	0.9863	0.0021	0.0004	0.0027	1.5027	9.52
VCA [49] + FCLS	0.9929	0.9977	0.9944	0.0016	0.0009	0.0022	1.8292	9.46
VCA [49] + MLMp [63]	0.9993	0.9932	0.9885	0.0032	0.0028	0.0026	1.8742	16.07
MVC-NMF [44] + NNLS	0.9904	0.9985	0.9739	0.0032	0.0025	0.0059	3.0210	1085.63
MVC-NMF [44] + FCLS	0.9912	0.9983	0.9878	0.0031	0.0025	0.0042	3.0450	1085.48
MVC-NMF [44] + MLMp [63]	0.9969	0.9999	0.9864	0.0046	0.0027	0.0023	2.0556	1093.57

3.3. Conclusions on the Experiments with Synthetic Data

The first experiment aims to test the sensitivity of the unmixing approaches with regard to the purity of the endmembers. According to the results shown in Section 3.1, it can be seen that when the spectra of the pixels are simple linear mixtures of the endmembers, VCA can produce robust results even when the pixels are highly mixed. The second experiment aims to evaluate the sensitivity of the approaches with regard to the spectral variations caused by non-linear effects (including observation geometries and grain sizes). According to the results shown in Section 3.2, for estimating the number of endmembers, it is the ELM method that can provide the most reasonable result. For the extraction of endmembers, VCA and MVC-NMF can both produce good spectral signatures. The abundances of the endmembers extracted by VCA and MVC-NMF are also coherent to the references. However, it has to be remarked that VCA is much more efficient than MVC-NMF with regard to the computation time.

4. Experiments and Results with Real Data

In the following section, experiments are carried out on a real hyperspectral image taken by the OMEGA instrument. This image is briefly introduced in Section 4.1. Its number of endmembers is estimated by ELM, HFC and HySime in Section 4.2. In Section 4.3, endmember spectra are extracted by VCA, SISAL and MVC-NMF and are then compared for identification with the reference spectra of the expected materials. Based on the spectra extracted by VCA, SISAL and MVC-NMF, the abundance maps are computed by NNLS and FCLS in Section 4.4. They are then compared with the abundances obtained by the state-of-the-art unmixing method BPSS, as presented in [31]. In Section 4.5, another comparison is performed, this time on a restricted area with the reference abundances obtained in [58] by inversion of a physical model. Finally, in Section 4.5, we summarize the results of linear unmixing obtained on the ORB0041image.

4.1. Dataset: The ORB0041 Image

The ORB0041 image (see Figure 5a) taken in late summer covers a large part of the south polar permanent cap (SPPC) and layered deposits of Mars. Prior to the analysis, it has been calibrated into reflectance factor units, but has not been corrected for atmospheric effects. We reduce the spatial extent of the image to this region of interest. Previous studies by [67] detected three principal chemically pure species on the surface: water ice, CO_2 ice and mineral dust. Physical analysis conducted independently by [13] on a selection of representative spectra showed that intimate mixtures of grains usually dominate the properties of the superficial icy deposits in the region. Furthermore, component abundance and granularity maps were computed by applying a Gaussian regularized sliced inverse regression (GRSIR) to the bright part of the SPPC of the image, trained with a library of synthetic spectra generated by a physical model [58]. The latter is built by assuming that the detected chemical components are intimately mixed. The ROI for the physical analysis of the ORB0041 image is shown in Figure 5b. The resulting abundances of H_2O ice, CO_2 ice and dust are shown in Figure 6. Being generated thanks to a more realistic model that takes into account the non-linear effects of the intimate mixture, the resulting abundances computed by GRSIR can serve as a reference for our experiment. Alternatively, [31] applied to the same OMEGA observation a blind source separation consisting of an ICA followed by a Bayesian scheme that implements positivity constraints. It has to be remarked that, in [31], the number of endmembers is manually fixed to three. The endmembers extracted by using VCA, SISAL and MVC-NMF are again identified by comparing their abundances with the abundances of the endmembers obtained in [31], which are shown in Figure 7.

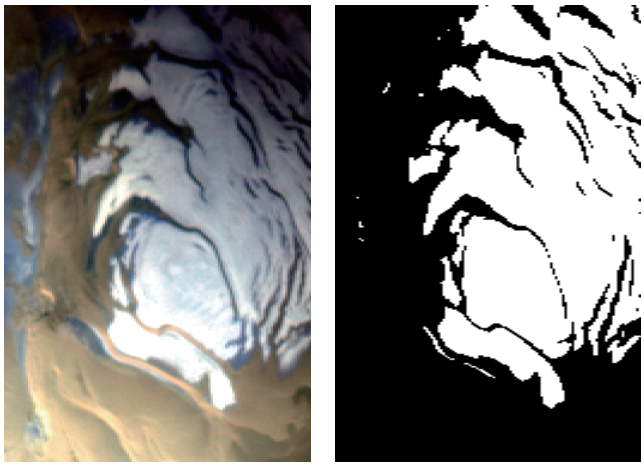

(**a**) (**b**)

Figure 5. (**a**) OMEGAORB0041image of the south pole of Mars. (R-band 100, G-band 50 and B-band 24); (**b**) ROI (in white), where the GRSIR has computed the physical parameters of the chemical components.

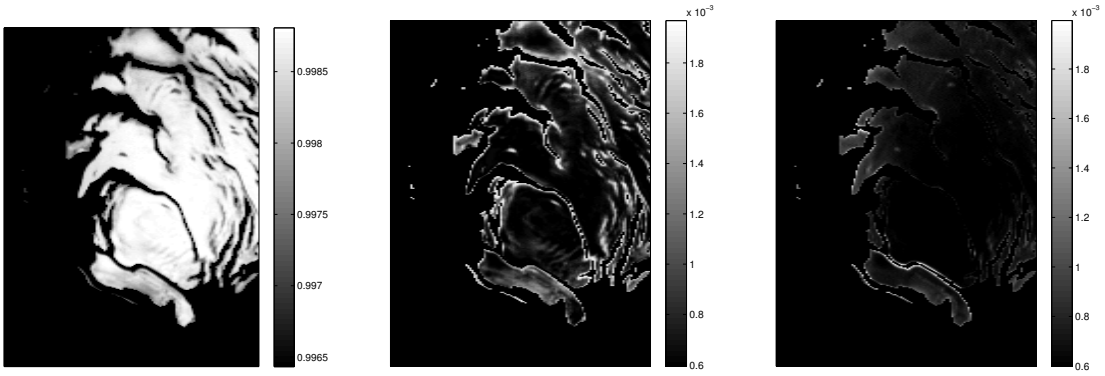

Figure 6. The abundances of the three endmembers computed by GRSIR [58], based on a physical model of the SPPC reflectivity.

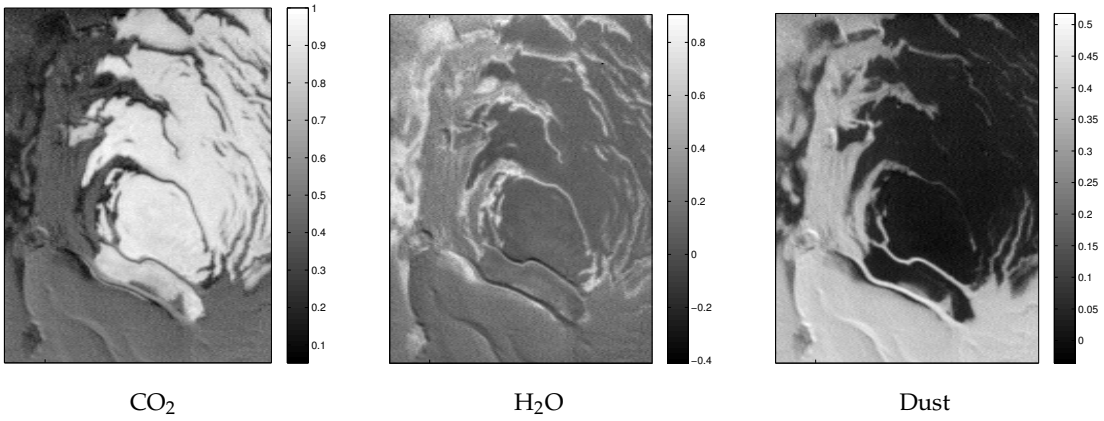

Figure 7. The abundances of the CO_2, H_2O and dust endmembers obtained by the state-of-the-art unmixing method presented in [31].

4.2. Estimation of the Number of Endmembers

First, we use ELM, HySime and HFC for estimating the number of endmembers in the ORB0041 image. The results are shown in Table 9.

Table 9. Numbers of endmembers estimated in the ORB0041 image by the use of the ELM, HySime and HFC methods.

	ELM [35]	**HySime [36]**	**HFC [34] ($\alpha = 10^{-3}$)**	**HFC [34] ($\alpha = 10^{-4}$)**	**HFC [34] ($\alpha = 10^{-5}$)**
estimated number	4	10	22	21	19

When we use the HySime method, the estimated number of endmembers is 10, which is considered too large, according to the previous studies. On the other hand, the numbers estimated by the HFC method are 22, 21 and 19, when $\alpha = 10^{-3}$, 10^{-4} and 10^{-5}, respectively. These numbers are also too large. Only ELM provides a realistic evaluation.

4.3. Extraction of the Endmembers

We extract four endmembers from image ORB0041 by using the VCA, SISAL and MVC-NMF methods (Figure 8). In order to identify the extracted spectra, the correlation coefficients and the

spectral angles between the latter and the reference spectra (see Figure 1) are computed (shown in Table 10). A spectroscopic visual inspection of the spectra is also carried out. Table 10 shows that the VCA method can extract mineral dust better than MVC-NMF and SISAL, while the MVC-NMF method can extract water ice better than VCA and SISAL. From a spectroscopic point of view, the quality of the dust endmembers extracted by VCA and MVC-NMF is excellent. In addition, the spectrum of dust extracted by SISAL is also plausible. Careful examinations of the spectra associated with the second and third endmembers lead to two different explanations for source splittings when one considers the VCA and the MVC-NMF outcomes. In the first case, the variation of the H_2O grain size can very well explain the spectral differences; whereas, in the second case, one can observe an intimate contamination by CO_2 ice for the second endmember, which is absent for the third one.

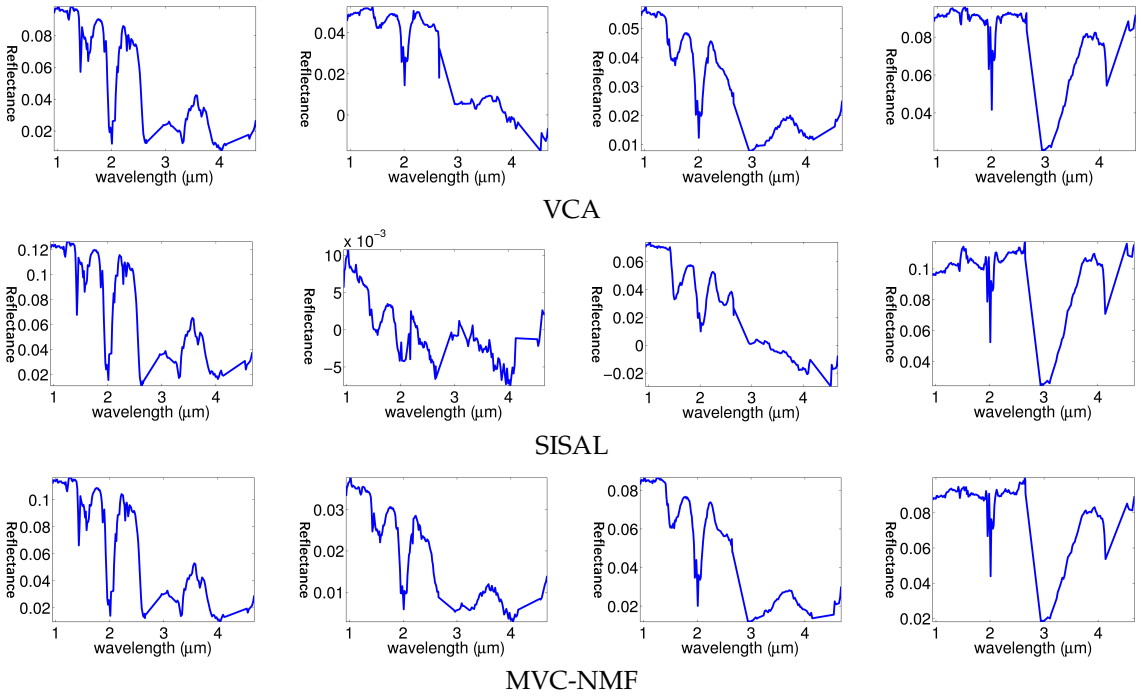

Figure 8. Spectra of the endmembers extracted, respectively, by VCA, SISAL and MVC-NMF from the ORB0041 image. The endmembers are sorted according to their chemical nature.

It can be seen that, although the third endmember extracted by SISAL can be visually identified as water ice, according to the correlation coefficient and the visual identification, the spectral angle between its spectrum and the reference spectrum of water ice is not the minimum (25.3 degrees). Meanwhile, the third endmembers extracted by both VCA and MVC-NMF correspond very well to water ice, according to the correlation coefficients and the spectral angles. In the previous section, it has been seen that the non-linear effects can split one physical source into several endmembers. From Table 10, we can see that the second endmembers extracted by VCA and MVC-NMF are also very similar to water ice (according to their high correlation coefficients and relatively small spectral angles). As for the CO_2 ice, according to the maximal correlation coefficients, it can be well extracted by all three methods. However, the minimal spectral angles between the reference spectrum of CO_2 ice and the extracted endmembers are relatively high (around 13–14 degrees) when compared to the equivalent values for the other endmembers. A difference in the dust contamination in the CO_2 ice between the reference and the extracted spectra can well account for this apparent lower adequacy, without questioning the physical quality of the produced CO_2 endmember by all three methods. According to Table 10, the VCA and MVC-NMF methods work better than SISAL on the ORB0041 image. The performances of VCA and MVC-NMF are very similar. However, it has to be noticed that

the computational complexity of MVC-NMF is considerably higher than VCA (VCA needs less than one second, compared to the half an hour required by MVC-NMF).

Table 10. Correlation coefficients and spectral angles between the reference spectra (in Figure 1) and the spectra of the endmembers extracted, respectively, by the use of VCA, SISAL and MVC-NMF with the ORB0041 image. A bold face stresses, in each case, the best result.

	Correlation Coefficient			Spectral Angle (degrees)		
			VCA [49]			
Endmember	**H_2O**	**CO_2**	**Dust**	**H_2O**	**CO_2**	**Dust**
1st	0.833	**0.959**	0.540	15.6	**13.2**	24.3
2nd	0.922	0.789	0.548	14.6	22.6	28.5
3rd	**0.933**	0.896	0.677	**8.79**	19.2	18.5
4th	0.835	0.503	**0.959**	14.9	33.8	**3.83**
			SISAL [53]			
1st	0.802	**0.952**	0.530	**16.1**	**14.6**	23.1
2nd	0.577	0.829	0.293	75.0	57.4	84.6
3rd	**0.898**	0.853	0.503	25.3	21.7	39.6
4th	0.657	0.246	**0.925**	18.3	37.3	**5.16**
			MVC-NMF [44]			
1st	0.825	**0.956**	0.530	15.9	**13.4**	24.4
2nd	0.884	0.937	0.606	13.0	15.0	22.8
3rd	**0.954**	0.865	0.664	**7.45**	20.2	19.3
4th	0.826	0.432	**0.946**	14.9	34.7	**4.38**

4.4. Extraction of the Abundances

In this section, we compute the abundance maps of the H_2O ice, CO_2 ice and the dust endmembers extracted by VCA, SISAL and MVC-NMF on the ORB0041 image. For each case, the abundance maps are estimated by the NNLS, FCLS and multilinear mixing model (MLMp [63]). According to Equation (7), the sum of the abundances estimated by NNLS is not necessarily equal to one (since the NNLS is not subjected to the sum-to-one condition). We can then perform an empirical normalization of the abundances estimated by NNLS with the following equation:

$$\hat{\mathbf{s}}_i^{Norm} = \frac{\hat{\mathbf{s}}_i}{\sum_{i=1}^{N_c} \hat{\mathbf{s}}_i}, \tag{13}$$

in order to force the sum of the abundances to be equal to one. This normalization also corresponds to a first-order correction of the photometric and shadow effects [68]. According to Equation (8), the sum of the abundances estimated by FCLS must be equal to one; therefore, such a normalization is not necessary for FCLS.

4.4.1. Abundance Maps of the Endmembers Extracted by VCA

We display in Figure 9 the abundances computed for the VCA endmembers, respectively, by using NNLS, NNLS after normalization by Equation (13), FCLS and MLMp. It can be seen that the normalization can satisfactorily correct the large-scale spatial variation that we note in the upper right corner of the maps for the abundances obtained by using NNLS (especially for the abundances of CO_2 ice). Such a variation is linked to the increasingly large values of incidence that are encountered in this part of the image. In contrast, applying the FCLS conditions makes the estimation of the abundances even more sensitive to the photometric effect.

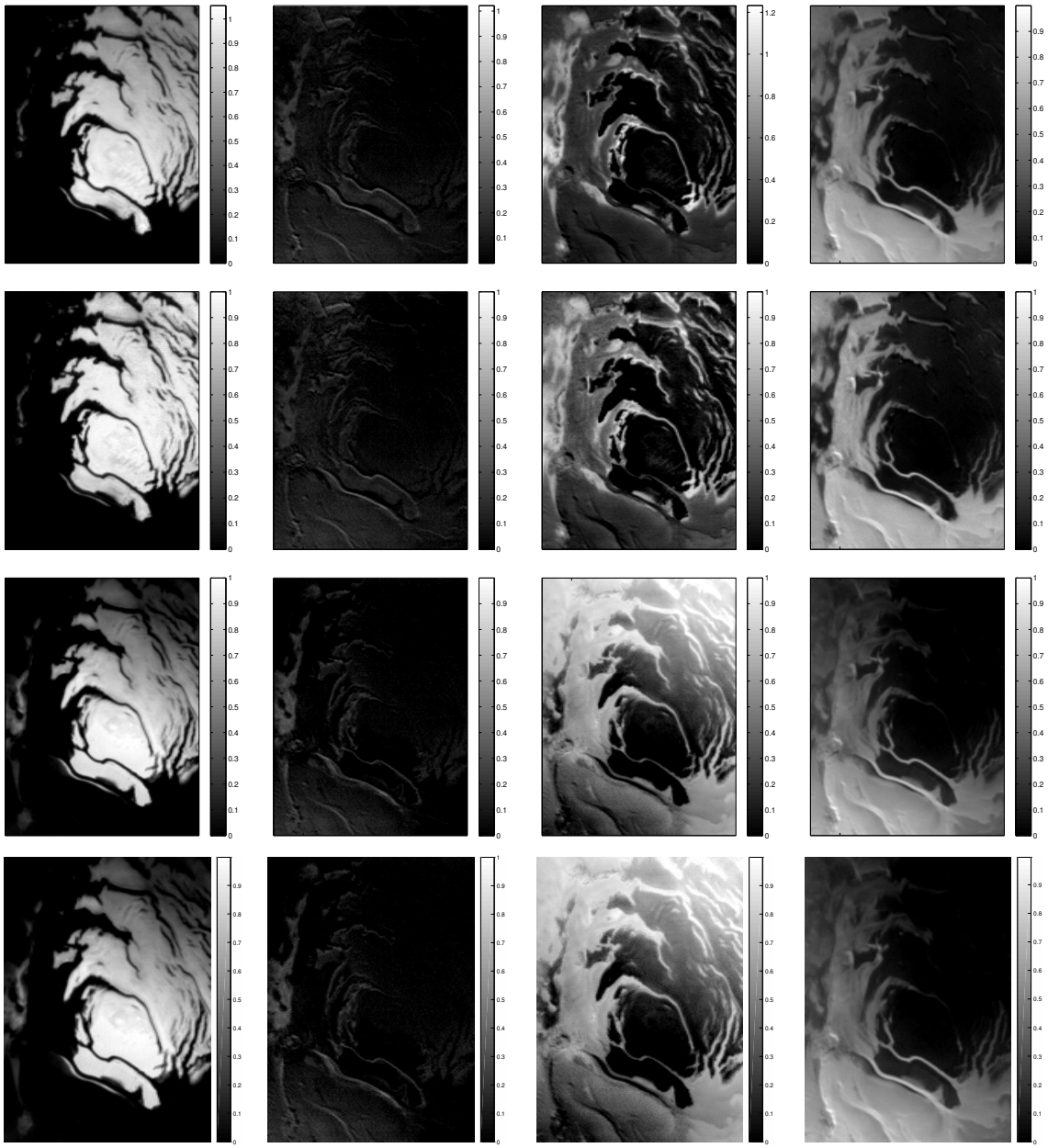

Figure 9. Abundance maps computed with the spectra of the endmembers extracted by VCA. The abundances are, respectively, estimated by the use of NNLS (first row), normalized NNLS abundances by the use of Equation (13) (second row), FCLS (third row) and MLMp (fourth row).

When we compare the abundance maps estimated by using NNLS with the abundance maps of water ice, CO_2 ice and mineral dust obtained in [31] (see Figure 7), it can be seen that the abundance maps of the 1st, 3rd and 4th endmembers, respectively, correspond to CO_2 ice, water ice and dust. This observation is coherent with the identification of the spectra of the endmembers (see Section 4.3). The abundance maps of the fourth and the first endmembers estimated by FCLS correspond well to dust and CO_2 ice. However, neither the second nor the third abundance maps are similar to the abundance of water ice.

4.4.2. Abundance Maps of the Endmembers Extracted by SISAL

With the help of the endmember spectra extracted by using SISAL, we then operate NNLS and FCLS in order to compute the abundance maps of the endmembers. The results of NNLS are also normalized by Equation (13). The results are shown in Figure 10.

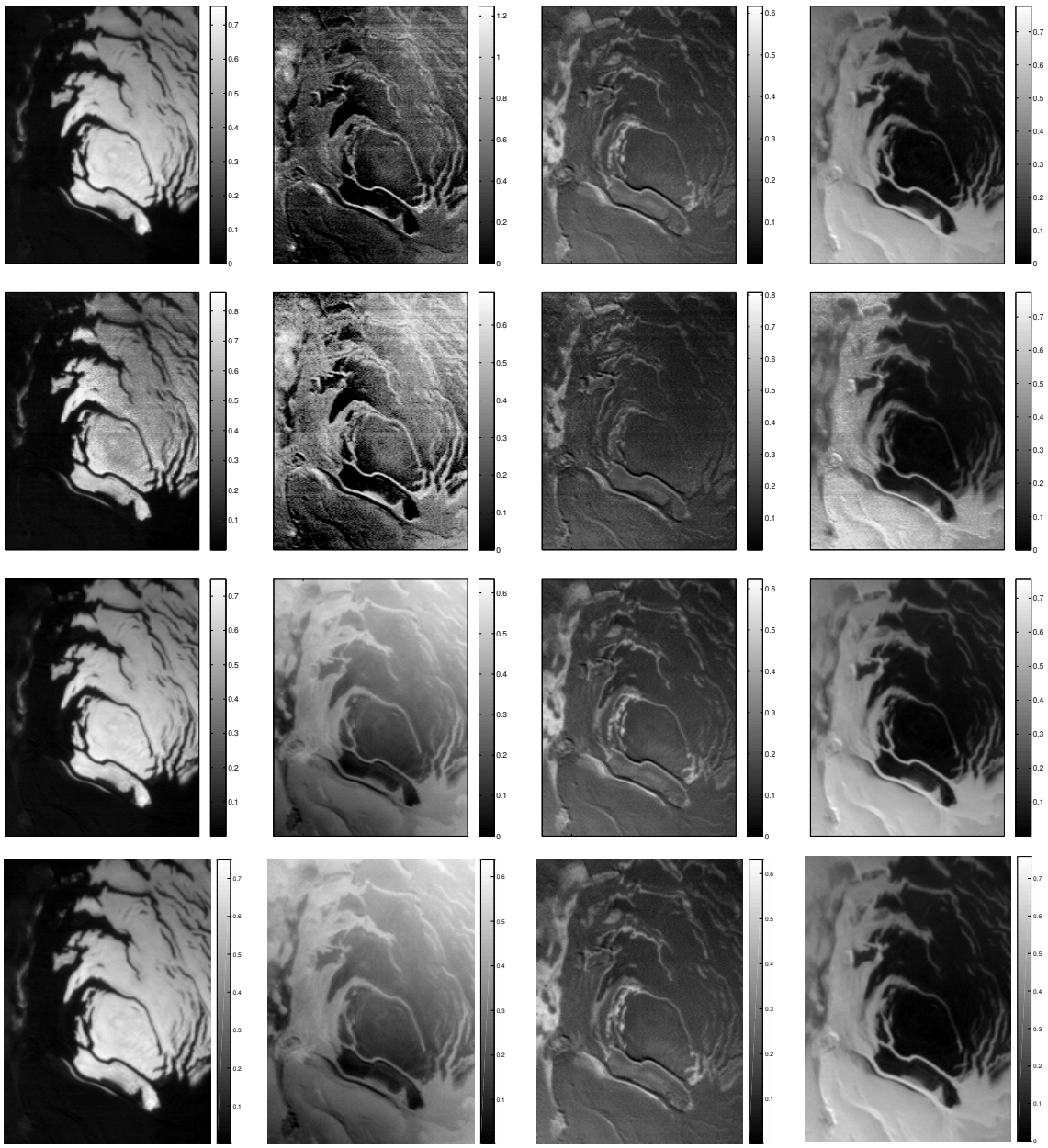

Figure 10. Abundance maps computed with the spectra of the endmembers extracted by SISAL. The abundances are, respectively, estimated by the use of NNLS (first row), normalized NNLS abundances by the use of Equation (13) (second row), FCLS (third row) and MLMp (fourth row).

When compared to the results in [31], it can be observed that the first and the fourth abundance maps estimated by each method (NNLS, FCLS and MLMp), respectively, correspond to CO_2 ice and dust, which is consistent with the identification of the spectra of the endmembers extracted by SISAL in Section 4.3. However, although the third abundance maps obtained by NNLS and FCLS are similar to the abundance of water ice, the background values are too high (more than 0.3), and the contrasts are very low. These results also conform to the identification of the spectra, since the correlation coefficient

of the most correlated endmember to the water ice extracted by SISAL is only 0.89 and the spectral angle is more than 20 degrees.

4.4.3. Abundance Maps of the Endmembers Extracted by MVC-NMF

With the help of the endmember spectra extracted by using MVC-NMF, we then operate NNLS, FCLS and MLMp in order to compute the abundance maps of the endmembers. The results of NNLS are also normalized by Equation (13). The results are shown in Figure 11.

The 1st, 3rd and 4th abundance maps, respectively, correspond to CO_2 ice, water ice and dust. This observation is consistent with the identification of the spectra in Section 4.3. The abundances estimated by FCLS are less noisy and more contrasted than the other maps, a tendency especially noticeable for water ice, for which the background abundance is relatively low.

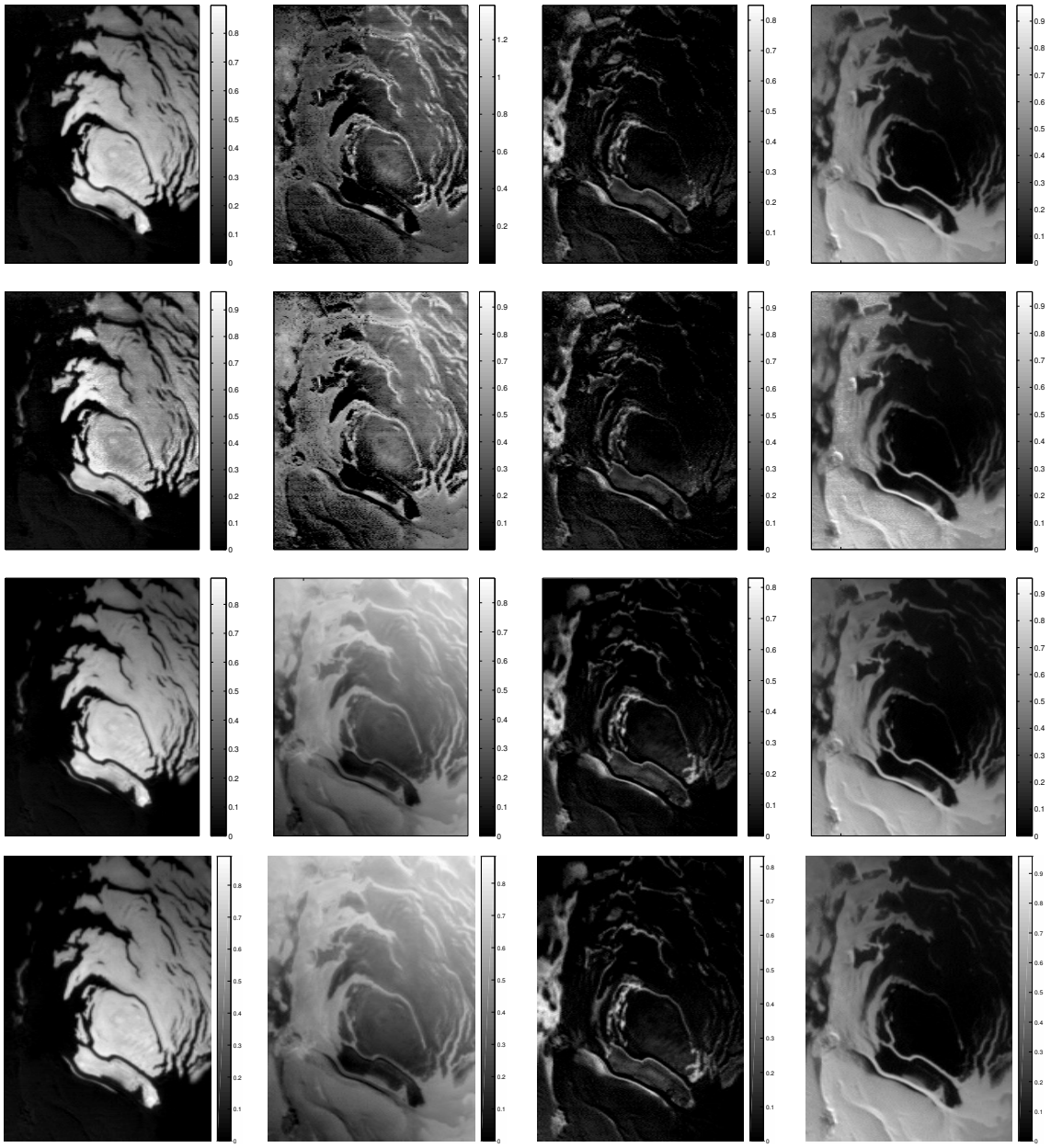

Figure 11. Abundance maps computed with the spectra of the endmembers extracted by MVC-NMF. The abundances are, respectively, estimated by the use of NNLS (first row), normalized NNLS abundances by the use of Equation (13) (second row), FCLS (third row) and MLMp (fourth row).

4.5. Validation of the Abundances

In the previous sections, we identified the extracted endmembers by comparing their spectra with the reference spectra and by visually comparing their abundances with those obtained by the method presented in [31]. We recall that the 1st, 3rd and 4th endmembers extracted by the VCA, SISAL and MVC-NMF methods are identified as CO_2 ice, H_2O ice and dust. In addition, according to Table 10, it has been observed that the second endmembers extracted by VCA and MVC-NMF might be additional endmembers related to water ice because of the source splitting effect. We have therefore added the abundance maps produced by VCA and MVC-NMF for the second and the third endmembers in order to map water ice. We now quantify the adequacy of the spatial distribution of the three compounds as depicted by the results of the selected unmixing methods with the reference abundance maps computed by GRSIR. The latter are shown in Figure 6. The correlation coefficients between the reference abundances and the abundances of the identified endmembers are shown in Table 11. It can be seen that the combination of abundances for the second and the third endmembers extracted by VCA and MVC-NMF generally improves the correlation coefficients. This confirms that combining these endmembers into a common water ice physical source is necessary to comprehend all the details of its spatial distribution.

Table 11. Unmixing performance of different models for the ORB0041 image: correlation coefficients, RE, MSE and time (in second). A bold face stresses, in each case, the best result (correlation coefficients between the abundances computed by the spectral unmixing and spectral index approaches and the reference abundances generated by GRSIR with a physical model).

Method	Correlation Coefficient				*RE*	*MSE*	Time (s)
	H_2O	H_2O (Combined)	Dust	CO_2			
VCA [49] + NNLS	0.820	0.842	0.871	0.729	**3.1495**	53.7838	**9.68**
VCA [49] + NNLS (normalized)	**0.827**	**0.877**	0.869	0.910	3.3439	**51.5418**	**9.68**
VCA [49] + FCLS	0.345	0.394	0.693	0.490	7.8934	91.4053	9.54
VCA [49] + MLMp [63]	0.348	0.388	0.685	0.492	5.6624	90.8815	16.88
SISAL [53] + NNLS	0.345	n/a	0.787	0.665	3.2110	73.3173	19.75
SISAL [53] + NNLS (normalized)	0.254	n/a	0.863	0.568	3.2628	73.3985	19.75
SISAL [53] + FCLS	0.374	n/a	0.845	0.665	3.4686	73.3424	19.12
SISAL [53] + MLMp [63]	0.384	n/a	0.854	0.664	3.7195	73.3374	29.83
MVC-NMF [44] + NNLS	0.411	0.576	0.887	0.657	3.2379	69.8420	1216.74
MVC-NMF [44] + NNLS (normalized)	0.394	0.581	**0.902**	0.616	3.4806	67.9421	1216.74
MVC-NMF [44] + FCLS	0.467	0.507	0.894	0.604	3.8670	70.1721	1216.36
MVC-NMF + MLMp [63]	0.468	0.510	0.894	0.605	3.7741	70.1235	1224.66
BPSS [40]	0.791	n/a	0.792	**0.941**	3.4463	130.9763	67.14
Spectral ratio	0.410	n/a	n/a	0.790	n/a	n/a	n/a

The work in [12] proposed two spectral indices suitable for obtaining, in a relative sense, the spatial distribution of H_2O and CO_2 ices while minimizing the influence of the acquisition geometry and the atmospheric contribution to the signal. In order to contrast the relative accuracy of the latter approach, we compute the H_2O and CO_2 ratio maps for the observation ORB0041 and estimate their correlation coefficients with the reference. Table 11 illustrates the possibility of using linear unmixing methods instead of spectral indices, beyond the fact that the former are unsupervised. Indeed, the H_2O index, for instance, fails to satisfactorily reproduce the spatial distribution of H_2O ice on the polar cap. Furthermore, an index for dust cannot be put forward. The CO_2 index, on the other hand, gives more reliable results, although they are not optimal.

Discussion of the Experiments with the ORB0041 Image

According to the unmixing results obtained with the ORB0041 image, the following conclusions can be drawn:

- The number of endmembers estimated by using the ELM method is more reasonable than the one obtained by both the HySime and the HFC methods, which is coherent with the results obtained from synthetic data in Section 3.2.
- The endmember spectra extracted by VCA and MVC-NMF are more correlated to the reference spectra than SISAL. All three chemical components (water ice, CO_2 ice and mineral dust) can be clearly identified when VCA and MVC-NMF are used.
- It has to be noted that VCA directly extracts the extremal points as endmembers, while MVC-NMF has to solve an optimization problem. Therefore, the computational complexity of MVC-NMF is considerably higher than VCA. In order to extract four endmembers from the ORB0041 image, VCA needs less than one second, while MVC-NMF takes around 20 min on a machine with an Intel I3 540 CPU and 6 GHz of memory. This can be a key issue when analyzing large series of OMEGA images.
- The combination of VCA + NNLS provides the best abundance maps for the three major compounds of the south pole of Mars, provided that the abundances have been normalized after the unmixing by using Equation (13). Consequently, adding the sum-to-one condition (FCLS) directly in the unmixing step does not always improve the unmixing results. Following [68], we explain this fact by mentioning the frequent presence of shadows in orbital images at the sub-pixel level due to small-scale topography. The pixel fraction occupied by shadows can be especially large at high latitudes (such as in the case of the ORB0041 image), for which typical sun elevations are low. As they are often spectrally correlated with another endmember (dust in our case), shadows cannot appear as independent endmembers themselves, but are nevertheless present. The effective endmembers are "extremes" (i.e., they contain less shadow proportion) compared to the rest of the spectra. Consequently, to account for shadows inside the simplex, it is better not to impose the sum-to-one condition while the positivity is relevant, as confirmed in this experiment.
- Even though the unmixing is based on a very simple linear model, it can provide a similar relative spatial distribution of the materials to that achieved by a complete physical analysis, which requires complex physical models and much a priori information about the compounds. Conversely, the linear unmixing approaches used in this article are unsupervised and parameter free. In addition, the computational complexity of the linear unmixing approaches is very low. A typical combination of ELM + VCA + NNLS, which covers the complete unmixing chain, requires only a few seconds.
- We do not have an absolute ground truth regarding the state of the southern permanent polar cap. Nonetheless, the abundance maps obtained by the best unmixing methods and the physical maps show very satisfactory relative agreement. On the contrary, the correlation between abundance maps obtained by spectral indices and physical maps is relatively low. This indicates that the approach of spectral indices is not reliable when an intimate mixture of compounds prevails.

5. Conclusions

In this article, the capability of a chain of unsupervised linear unmixing applied to the analysis of synthetic, as well as real hyperspectral images is investigated in the framework of a Martian case study. For each of the three steps in the linear unmixing chain, several methods are evaluated. For the first step, the estimation of the number of endmembers, the ELM, HySime and HFC methods are compared. For the second step the extraction of endmembers, the VCA, SISAL and MVC-NMF methods, each representing a major category of geometrical approach, are selected for evaluation. For the third step, the linear unmixing of hyperspectral data, the NNLS and FCLS conditions are tested. Three different datasets are used for evaluating the chain: synthetic data simulated strictly according to a linear mixture model,

synthetic data simulated by a more realistic model with non-linearities caused by photometric and grain size variations and a real image from ORB0041 acquired by the OMEGA instrument.

Because the synthetic data of the first experiment are simulated strictly by the linear mixture model, all methods of each step provide very similar results, except when the endmembers are highly mixed (i.e., the maximal abundance of each endmember is only 0.6). In this case, the VCA method still provides relatively good endmembers, while the other two methods fail. Thus, in the highly-mixed case, the SISAL method, which does not require the pure pixel assumption, can extract distorted endmembers that are unphysical. In all likelihood, SISAL will then not be robust against the presence of outlier spectra and of significant levels of noise for some channels, a situation often encountered in planetary hyperspectral data. On the other hand, because the VCA method is based on the pure pixel assumption, it always proposes endmembers that exist in the image; although they may actually be mixed spectra, they are more likely to be approximately relevant.

With the synthetic data of the second experiment, only ELM provides a reasonable number of endmembers, while HySime and HFC overestimate this parameter. The VCA + NNLS, VCA + FCLS, MVC-NMF + NNLS and MVC-NMF + FCLS methods all provide good endmember signatures. However, the spectral unmixing of the data is affected by source splitting linked with the non-linear spectral effects, thus making necessary the recombination of the extracted endmembers into a lower number of real physical sources. The abundance map of a given physical source is then obtained by adding the individual abundances of the associated endmembers. Such a recombination could be a hurdle in an automatic processing pipeline if it were performed manually. Consequently, we suggest two possible remedies: (i) work out a recombination based on an unsupervised analysis of the nature of the endmembers; or (ii) include an atmospheric and a photometric correction step prior to the spectral unmixing, if feasible, to decrease the probability of source splitting. On the other hand, source splitting due to the intrinsic variability of the physical properties of a given compound could be considered satisfactory as it is, if one accepts getting the spatial distribution of its different forms separately. We should note also that FCLS is systematically slightly better than NNLS because, although non-linearities exist in the synthetic data, there is only a limited number of physical sources and no shadow is present in the data. In such a situation, the application of the sum-to-one condition can improve the precision of the results.

On the real image of the south pole of Mars acquired at high latitudes by the OMEGA instrument, ELM is the only method that provides a reasonable number of endmembers. The VCA + NNLS (normalized) method gives the best endmember signatures and abundances, while applying the FCLS condition leads to degraded results. This is because the latter condition does not allow us to take the contribution of shadows properly into account in the spectral signal. In contrast, VCA + NNLS (normalized) compares well with a state-of-the art unmixing approach (BPSS) and with the outcome of a complete physical analysis. The latter is performed by the inversion of a physical model that offers a more accurate simulation of the signal, but requires a lot more a priori information. Conversely, the unsupervised chain is nearly automatic, not requiring any prior information, notwithstanding the possible requirement of endmember recombination into actual physical sources should non-linear effects be noticeable. In addition, a physical model usually pertains to a given terrain unit among others (in our case, the bright part of the SPPC spectrally dominated by CO_2 ice), while the unsupervised unmixing chain can extract the spectra and provide the abundances of the compounds on the whole image. The drawback of simplicity and efficiency is that unsupervised linear unmixing usually provides the relative spatial variations of compound abundances, not absolute values. This is comparable to the classical spectral index methods, but our study has shown that the latter, in contrast with the unmixing, do not even satisfactorily reproduce the relative spatial distribution when intimate mixtures prevail, which is the usual situation on planetary surfaces.

All the previous elements lead to the general conclusion that the ELM + VCA + NNLS combination offers the best compromise in terms of accuracy and efficiency. Because it requires only a few seconds to process an OMEGA image or equivalent imagery, the unsupervised unmixing chain we have proposed

has great potential for the planetary exploration of large image series, at least if they contain ices with distinct and strong signatures, similar to our case study. In the Martian case, this may be a key asset for the systematic exploitation of the OMEGA and CRISM (compact reconnaissance imaging spectrometer for Mars) datasets at high latitudes.

Author Contributions: B.L. conceived of and designed the experiments. J.L. and B.L. performed the experiments, analyzed the data and wrote the paper. S.D. and J.C. gave valuable comments and suggestions and carefully revised the manuscript.

Acknowledgments: This work was undertaken under the framework of Project 61261130587 and 61571332 supported by NSFC. This work is also supported by the ANR-NSFC joint funded project I2-MARS.

Conflicts of Interest: The authors declare no conflict of interest.

Abbreviations

The following abbreviations are used in this manuscript:

OMEGA	Observatoire pour la Minéralogie, l'Eau, les Glaces et l'Activité
HFC	Harsanyi–Farrand–Chan
ELM	eigenvalue likelihood maximization
NMF	non-negative matrix factorization
PCA	principal component analysis
ICA	independent component analysis
BPSS	Bayesian positive source separation
MVC-NMF	minimum-volume constrained non-negative matrix factorization
VCA	vertex component analysis
SMACC	sequential maximum angle convex cone
KLF	Kalman filter
MVES	minimum-volume enclosing simplex
SISAL	simplex identification via split augmented Lagrangian
MVSA	minimum-volume simplex analysis
NNLS	non-negativity condition least squares error estimators
FCLS	full condition least squares error estimators
UCLS	unconditioned least squares error estimators
SNR	signal to noise ratio
SPPC	south polar permanent cap
GRSIR	Gaussian regularized sliced inverse regression
ROI	region of interest
MLMp	proposed multilinear mixing models

References

1. Christensen, P.R.; Anderson, D.L.; Chase, S.C.; Clancy, R.T.; Clark, R.N.; Conrath, B.J.; Kieffer, H.H.; Kuzmin, R.O.; Malin, M.C.; Pearl, J.C.; et al. Results from the Mars Global Surveyor Thermal Emission Spectrometer. *Science* **1998**, *279*, 1692–1698. [CrossRef] [PubMed]
2. Clark, R.N.; Hoefen, T.M. Spectral Feature Mapping with Mars Global Surveyor Thermal Emission Spectra: Mineralogic Implications. In *Bulletin of the American Astronomical Society*; DPS Meeting Abstract 32; American Astronomical Society: Washington, DC, USA, 2000; Volume 32, p. 1118.
3. Christensen, P.R.; Anderson, D.L.; Chase, S.C.; Clark, R.N.; Kieffer, H.H.; Malin, M.C.; Pearl, J.C.; Carpenter, J.; Bandiera, N.; Brown, F.G.; et al. Thermal emission spectrometer experiment: Mars Observer mission. *J. Geophys. Res. Planets* **1992**, *97*, 7719–7734. [CrossRef]
4. Carlson, R.; Smythe, W.; Baines, K.; Barbinis, E.; Becker, K.; Burns, R.; Calcutt, S.; Calvin, W.; Clark, R.; Danielson, G.; et al. Near-infrared spectroscopy and spectral mapping of Jupiter and the Galilean satellites: Results from Galileo's initial orbit. *Science* **1996**, *274*, 385–388. [CrossRef] [PubMed]

5. Coradini, A.; Filacchione, G.; Capaccioni, F.; Cerroni, P.; Adriani, A.; Brown, R.; Langevin, Y.; Gondet, B. CASSINI/VIMS-V at Jupiter: Radiometric calibration test and data results. *Planet. Space Sci.* **2004**, *52*, 661–670. [CrossRef]
6. Marty, B.; Guillot, T.; Coustenis, A.; Achilleos, N.; Alibert, Y.; Asmar, S.W.; Atkinson, D.; Atreya, S.K.; Babasides, G.; Baines, K.; et al. Kronos: Exploring the depths of Saturn with probes and remote sensing through an international mission. *Exp. Astron.* **2009**, *23*, 947–976. [CrossRef]
7. Nozette, S.D.; Spudis, P.D.; Robinson, M.S.; Bussey, D.B.J.; Lichtenberg, C.; Bonner, R. Integration of Lunar Polar Remote-Sensing Data Sets: Evidence for Ice at the Lunar South Pole. *J. Geophys. Res.* **2001**, *106*, 23253–23266. [CrossRef]
8. Pieters, C.M.; Tompkins, S. Remote Sensing of Lunar Mineralogy: The Glass Conundrum. In Proceedings of the 36th Annual Lunar and Planetary Science Conference, League City, TX, USA, 14–18 March 2005; Mackwell, S., Stansbery, E., Eds.; 2005; Volume 36.
9. Bibring, J.P.; Soufflot, A.; Berthé, M.; Langevin, Y.; Gondet, B.; Drossart, P.; Bouyé, M.; Combes, M.; Puget, P.; Semery, A. OMEGA: Observatoire pour la Minéralogie, l'Eau, les Glaces et l'Activité. In *Mars Express: The Scientific Payload*; ESA SP-1240; ESA Publications Division: Noordwijk, The Netherlands, 2004.
10. Bibring, P.J.; Langevin, Y.; Gendrin, A.; Gondet, B.; Poulet, F.; Berthé, M.; Soufflot, A.; Arvidson, R.; Mangold, N.; Mustard, J.; et al. Mars Surface Diversity as Revealed by the OMEGA/Mars Express Observations. *Science* **2005**, *307*, 1576–1581. [CrossRef] [PubMed]
11. Bibring, J.P.; Langevin, Y.; Mustard, J.F.; Poulet, F.; Arvidson, R.; Gendrin, A.; Gondet, B.; Mangold, N.; Pinet, P.; Forget, F. Global Mineralogical and Aqueous Mars History Derived from OMEGA/Mars Express Data. *Science* **2006**, *312*, 400–404. [CrossRef] [PubMed]
12. Langevin, Y.; Bibring, J.P.; Montmessin, F.; Forget, F.; Vincendon, M.; Douté, S.; Poulet, F.; Gondet, B. Observations of the south seasonal cap of Mars during recession in 2004–2006 by the OMEGA visible/near-infrared imaging spectrometer on board Mars Express. *J. Geophys. Res.* **2007**, *112*. [CrossRef]
13. Douté, S.; Schmitt, B.; Langevin, Y.; Bibring, J.P.; Altieri, F.; Bellucci, G.; Gondet, B.; Poulet, F. South Pole of Mars: Nature and composition of the icy terrains from Mars Express OMEGA observations. *Planet. Space Sci.* **2007**, *55*, 113–133. [CrossRef]
14. Appéré, T.; Schmitt, B.; Langevin, Y.; Douté, S.; Pommerol, A.; Forget, F.; Spiga, A.; Gondet, B.; Bibring, J.P. Winter and spring evolution of northern seasonal deposits on Mars from OMEGA on Mars Express. *J. Geophys. Res.* **2011**, *116*, E05001. [CrossRef]
15. Schmidt, F.; Douté, S.; Schmitt, B.; Vincendon, M.; Bibring, J.P.; Langevin, Y.; Team, T. Albedo control of seasonal South Polar cap recession on Mars. *Icarus* **2009**, *200*, 374–394. [CrossRef]
16. Pompilio, L.; Sgavetti, M.; Pedrazzi, G. Visible and near-infrared reflectance spectroscopy of pyroxene-bearing rocks: New constraints for understanding planetary surface compositions. *J. Geophys. Res.* **2007**, *112*, doi:10.1029/2006JE002737. [CrossRef]
17. Plaza, A.; Martinez, P.; Perez, R.; Plaza, J. A quantitative and comparative analysis of endmember extraction algorithms from hyperspectral data. *IEEE Trans. Geosci. Remote Sens.* **2004**, *44*, 650–663. [CrossRef]
18. Bioucasdias, J.M.; Plaza, A.; Dobigeon, N.; Parente, M.P.L.; Du, Q.; Gader, P.D.; Chanussot, J. Hyperspectral Unmixing Overview: Geometrical, Statistical, and Sparse Regression-Based Approaches. *IEEE J. Sel. Top. Appl. Earth Observ. Remote Sens.* **2012**, *5*, 354–379. [CrossRef]
19. Ma, W.; Bioucasdias, J.M.; Chan, T.; Gillis, N.; Gader, P.D.; Plaza, A.; Ambikapathi, A.; Chi, C. A Signal Processing Perspective on Hyperspectral Unmixing: Insights from Remote Sensing. *IEEE Signal Process. Mag.* **2014**, *31*, 67–81. [CrossRef]
20. Liangrocapart, S.; Petrou, M. Mixed pixels classification. *Remote Sens.* **1998**, *3500*, 72–83.
21. Keshava, N.; Mustard, J.F. Spectral unmixing. *IEEE Signal Process. Mag.* **2002**, *19*, 44–57. [CrossRef]
22. Parente, M.; Plaza, A. Survey of Geometric and Statistical Unmixing Algorithms for Hyperspectral Images. In Proceedings of the IEEE GRSS Workshop on Hyperspectral Image and Signal Processing: Evolution in Remote Sensing (WHISPERS10), Reykjavik, Iceland, 14–16 June 2010; pp. 1–4.
23. Huck, A.; Guillaume, M.; Blanc-Talon, J. Minimum Dispersion Constrained Nonnegative Matrix Factorization to Unmix Hyperspectral Data. *IEEE Trans. Geosci. Remote Sens.* **2010**, *48*, 2590–2602. [CrossRef]
24. Altmann, Y.; Mclaughlin, S.; Hero, A.O. Robust Linear Spectral Unmixing Using Anomaly Detection. *IEEE Trans. Comput. Imaging* **2015**, *1*, 74–85. [CrossRef]

25. Li, J.; Agathos, A.; Zaharie, D.; Bioucasdias, J.M.; Plaza, A.; Li, X. Minimum Volume Simplex Analysis: A Fast Algorithm for Linear Hyperspectral Unmixing. *IEEE Trans. Geosci. Remote Sens.* **2015**, *53*, 5067–5082.
26. Heylen, R.; Parente, M.P.L.; Gader, P.D. A Review of Nonlinear Hyperspectral Unmixing Methods. *IEEE J. Sel. Top. Appl. Earth Obs. Remote Sens.* **2014**, *7*, 1844–1868. [CrossRef]
27. Dobigeon, N.; Tourneret, J.; Richard, C.; Bermudez, J.C.M.; Mclaughlin, S.; Hero, A.O. Nonlinear Unmixing of Hyperspectral Images: Models and Algorithms. *IEEE Signal Process. Mag.* **2014**, *31*, 82–94. [CrossRef]
28. Halimi, A.; Honeine, P.; Bioucasdias, J.M. Hyperspectral Unmixing in Presence of Endmember Variability, Nonlinearity, or Mismodeling Effects. *IEEE Trans. Image Process.* **2016**, *25*, 4565–4579. [CrossRef] [PubMed]
29. Kalaitzis, A.A.; Lawrence, N.D. Residual Components Analysis. In Proceedings of the International Conference on Machine Learning, Edinburgh, UK, 26 June–1 July 2012.
30. Halimi, A.; Bioucasdias, J.M.; Dobigeon, N.; Buller, G.S.; Mclaughlin, S. Fast Hyperspectral Unmixing in Presence of Nonlinearity or Mismodeling Effects. *IEEE Trans. Comput. Imaging* **2017**, *3*, 146–159. [CrossRef]
31. Moussaoui, S.; Hauksdottir, H.; Schmidt, F.; Jutten, C.; Chanussot, J.; Brie, D.; Douté, S.; Benediktsson, J.A. On the decomposition of Mars hyperspectral data by ICA and Bayesian positive source separation. *Neurocomputing* **2008**, *71*, 2194–2208. [CrossRef]
32. Ceamanos, X.; Douté, S.; Luo, B.; Schmidt, F.; Jouannic, G.; Chanussot, J. Intercomparison and Validation of Techniques for Spectral Unmixing of Hyperspectral Images: A Planetary Case Study. *IEEE Trans. Geosci. Remote Sens.* **2011**, *49*, 4341–4358. [CrossRef]
33. Guerra, R.; Santos, L.; López, S.; Sarmiento, R. A New Fast Algorithm for Linearly Unmixing Hyperspectral Images. *IEEE Trans. Geosci. Remote Sens.* **2015**, *53*, 6752–6765. [CrossRef]
34. Chang, C.I.; Du, Q. Estimation of number of spectrally distinct signal Sources in Hyperspectral Imagery. *IEEE Trans. Geosci. Remote Sens.* **2004**, *42*, 608–619. [CrossRef]
35. Luo, B.; Chanussot, J.; Doute, S.; Zhang, L. Empirical Automatic Estimation of the Number of Endmembers in Hyperspectral Images. *IEEE Geosci. Remote Sens. Lett.* **2013**, *10*, 24–28.
36. Bioucas-Dias, J.M.; Nascimento, J.M.P. Hyperspectral Subspace Identification. *IEEE Trans. Geosci. Remote Sens.* **2008**, *46*, 2435–2445. [CrossRef]
37. Chevrel, S.; Pinet, P.; Daydou, Y.; Mouélic, S.L.; Langevin, Y.; Costard, F.; Erard, S. The Aristarchus Plateau on the Moon: Mineralogical and structural study from integrated Clementine UV-Vis-NIR spectral data. *Icarus* **2009**, *199*, 9–24. [CrossRef]
38. Nascimento, J.; Dias, J.B. Does independent component analysis play a role in unmixing hyperspectral data. *IEEE Trans. Geosci. Remote Sens.* **2005**, *43*, 175–187. [CrossRef]
39. Forni, O.; Poulet, F.; Bibring, J.P.; Erard, S.; Gomez, C.; Langevin, Y.; Gondet, B.; The OMEGA Science Team. Component Separation of OMEGA Spectra with ICA. In Proceedings of the 36th Lunar and Planetary Science Conference, League City, TX, USA, 15–19 March 2005.
40. Moussaoui, S.; Brie, D.; Mohammad-Djafari, A.; Carteret, C. Separation of Non-Negative Mixture of Non-Negative Sources Using a Bayesian Approach and MCMC Sampling. *IEEE Trans. Signal Process.* **2006**, *54*, 4133–4145. [CrossRef]
41. Lee, D.; Seung, H.S. Learning the parts of objects by non-negative matrix factorization. *Nature* **1999**, *401*, 788–791. [PubMed]
42. Zhao, C.; Zhao, G.; Jia, X. Hyperspectral Image Unmixing Based on Fast Kernel Archetypal Analysis. *IEEE J. Sel. Top. Appl. Earth Obs. Remote Sens.* **2017**, *10*, 331–346. [CrossRef]
43. Lu, X.; Wu, H.; Yuan, Y.; Yan, P.; Li, X. Manifold Regularized Sparse NMF for Hyperspectral Unmixing. *IEEE Trans. Geosci. Remote Sens.* **2013**, *51*, 2815–2826. [CrossRef]
44. Miao, L.; Qi, H. Endmember extraction from highly mixed data using minimum volume constrained nonnegative matrix factorization. *IEEE Trans. Geosci. Remote Sens.* **2007**, *45*, 765–777. [CrossRef]
45. Qu, Q.; Nasrabadi, N.M.; Tran, T.D. Subspace Vertex Pursuit: A Fast and Robust Near-Separable Nonnegative Matrix Factorization Method for Hyperspectral Unmixing. *IEEE J. Sel. Top. Signal Process.* **2015**, *9*, 1142–1155. [CrossRef]
46. Wang, W.; Qian, Y.; Tang, Y.Y. Hypergraph-Regularized Sparse NMF for Hyperspectral Unmixing. *IEEE J. Sel. Top. Appl. Earth Obs. Remote Sens.* **2016**, *9*, 681–694. [CrossRef]

47. Parente, M.; Bishop, J.; Bell, J., III. Spectral unmixing for mineral identification in Pancam images of soils in Gusev crater, Mars. *Icarus* **2009**, *203*, 421–436. [CrossRef]
48. Winter, M.E. Fast autonomous spectral end-member determination. In Proceedings of the 13th International Conference on Applied Geologic Remote Sensing, Vancouver, BC, Canada, 1–3 March 1999; Volume 2, pp. 337–344.
49. Nascimento, J.; Dias, J.B. Vertex component analysis: A fast algorithm to unmix hyperspectral data. *IEEE Trans. Geosci. Remote Sens.* **2005**, *43*, 898–910. [CrossRef]
50. Gruninger, J.; Ratkowski, A.J.; Hoke, M.L.; Shen, S.S.; Lewis, P.E. The sequential maximum angle convex cone (SMACC) endmember model. In *Algorithms and Technologies for Multispectral, Hyperspectral, and Ultraspectral Imagery X*; International Society for Optics and Photonics: Orlando, FL, USA, 2004; Volume 5425, pp. 1–14.
51. Li, J.; Bioucas-Dias, J.M. Minimum Volume Simplex Analysis: A Fast Algorithm to Unmix Hyperspectral Data. In Proceedings of the IEEE International 2008 Geoscience and Remote Sensing Symposium, Boston, MA, USA, 6–11 July 2008; Volume 3.
52. Chan, T.; Chi, C.; Huang, Y.; Ma, W. A convex analysis-based minimum-volume enclosing simplex algorithm for hyperspectral unmxing. *IEEE Trans. Signal Process.* **2009**, *57*, 4418–4432. [CrossRef]
53. Bioucas-Dias, J. A variable splitting augmented Lagrangian approach to linear spectral unmixing. In Proceedings of the First IEEE GRSS Workshop on Hyperspectral Image and Signal Processing, Grenoble, France, 26–28 August 2009; pp. 1–4.
54. Boardman, J.W. Mapping Target Signatures via Partial Unmixing of AVIRIS Data. In *Summaries of Jpl Airborne Geoscience Workshop*; JPL Publication: Pasadena, CA, USA, 1995; Volume 1, pp. 23–26.
55. Qian, Y.; Jia, S.; Zhou, J.; Robleskelly, A. Hyperspectral Unmixing via $L_{1/2}$ Sparsity-Constrained Nonnegative Matrix Factorization. *IEEE Trans. Geosci. Remote Sens.* **2011**, *49*, 4282–4297. [CrossRef]
56. Poulet, F.; Bibring, J.P.; Langevin, Y.; Mustard, J.F.; Mangold, N.; Vincendon, M.; Gondet, B.; Pinet, P.; Bardintzeff, J.M.; Platevoet, B. Quantitative compositional analysis of martian mafic regions using the MEx/OMEGA reflectance data. *Icarus* **2009**, *201*, 69–83. [CrossRef]
57. Poulet, F.; Arvidson, R.E.; Gomez, C.; Morris, R.V.; Bibring, J.P.; Langevin, Y.; Gondet, B.; Griffes, J. Mineralogy of Terra Meridiani and western Arabia Terra from OMEGA/MEx and implications for their formation. *Icarus* **2008**, *195*, 106–130. [CrossRef]
58. Bernard-Michel, C.; Douté, S.; Fauvel, M.; Gardes, L.; Girard, S. Retrieval of Mars surface physical properties from OMEGA hyperspectral images using Regularized Sliced Inverse Regression. *J. Geophys. Res.* **2009**, *114*. [CrossRef]
59. Neyman, J.; Pearson, E.S. On the Problem of the Most Efficient Tests of Statistical Hypotheses. *Philos. Trans. R. Soc. Lond. Ser. A Contain. Pap. Math. Phys. Charact.* **1933**, *231*, 289–337. [CrossRef]
60. Anderson, T. *An Introduction to Multivariate Statistical Analysis*, 2nd ed.; Springer: New York, NY, USA, 1984.
61. Heinz, D.C.; Chang, C.I. Fully constrained least squares linear spectral mixture analysis method for material quantification in hyperspectral imagery. *IEEE Trans. Geosci. Remote Sens.* **2001**, *39*, 529–545. [CrossRef]
62. Heylen, R.; Scheunders, P. A Multilinear Mixing Model for Nonlinear Spectral Unmixing. *IEEE Trans. Geosci. Remote Sens.* **2016**, *54*, 240–251. [CrossRef]
63. Wei, Q.; Chen, M.; Tourneret, J.Y.; Godsill, S. Unsupervised Nonlinear Spectral Unmixing Based on a Multilinear Mixing Model. *IEEE Trans. Geosci. Remote Sens.* **2017**, *55*, 4534–4544. [CrossRef]
64. Christensen, P.R.; Bandfield, J.L.; Bell, J.F.; Gorelick, N.; Hamilton, V.E.; Ivanov, A.B.; Jakosky, B.M.; Kieffer, H.H.; Lane, M.D.; Malin, M.C.; et al. Morphology and Composition of the Surface of Mars: Mars Odyssey THEMIS Results. *Science* **2003**, *300*, 2056–2061. [CrossRef] [PubMed]
65. Golombek, M.P. The Surface of Mars: Not Just Dust and Rocks. *Science* **2003**, *300*, 2043–2044. [CrossRef] [PubMed]
66. Schmidt, F.; Douté, S.; Schmidt, B. WAVANGLET: An efficient supervised classifier for hyperspectral images. *IEEE Trans. Geosci. Remote Sens.* **2007**, *45*, 1374–1385. [CrossRef]

67. Bibring, J.P.; Langevin, Y.; Poulet, F.; Gendrin, A.; Gondet, B.; Berthé, M.; Soufflot, A.; Drossart, P.; Combes, M.; Bellucci, G. Perennial water ice identified in the south polar cap of Mars. *Nature* **2004**, *428*, 627–630. [CrossRef] [PubMed]
68. Cord, A.; Pinet, P.; Daydou, Y.; Chevrel, S. Experimental determination of the surface photometric contribution in the spectral reflectance deconvolution processes for a simulated Martian crater-like regolithic target. *Icarus* **2006**, *175*, 78–91. [CrossRef]